Università degli Studi di Padova
Dipartimento di Fisica & Astronomia G. Galilei
Dipartimento di Ingegneria dell'informazione
Corso di laurea in Fisica

Tesi di Laurea Magistrale

Laser processes on surfaces in femtosecond domain

Relatore:
Prof. Paolo Villoresi

Corelatore:
Prof. Diego Tonini

Controrelatore:
Prof. Giovanni Carugno

Laureando: Elisa Appi
Matricola N: 1061562

Anno Accademico 2014-2015

Contents

Abstract

In this thesis we investigated the interaction between ultrafast pulses ($\leq 10\,\mathrm{ps}$) and nanometric dielectric surfaces. The study of the interaction between this kind of pulses and matter has a great importance in many types of application, principally for the reduced thermal effects and for the high precision achievable in the realized structures. Particularly, our work was interested in the solar industry application where an ultrafast laser source can be used to open the contacts in the passivation layer which covers the back side of the PERC solar cells. The study involved the characterization of the process in function of the surface, pulse length, different wavelengths and different average intensity. Subsequently the processed samples analysis with the use of SEM and EDX. The results have demonstrated that the removal of dielectric material can happen due to direct or indirect ablation and has highlighted the regimes in which there is a clean and precise delamination of the material without damaging the silicon substrate.
This study was realized thanks to the collaboration between Università degli Studi di Padova and Applied Material Italia that has financed the project and, especially, cared for the production and the testing of solar cells.

Chapter 1

Ultrafast laser.

Ultrafast laser sources are able to emit light pulses with a temporal width less than a few tens of picoseconds. Therefore, both femtoseconds and picoseconds sources are included in this class. The need of high precision machining and material processes with reduced thermal effects gave a boost to the development of this technology in the last three decades [1]. As a matter of fact, ultrafast lasers are now commonly used for the processing of materials in the field of fundamental research and, also, for pratical applications.
One of the most important features of the interaction between solid matter and ultrafast pulses is the reduction of diffused heat in the regions close to the processed area. This particular feature is due to the rapid transfer of energy to the material: when the temporal width of the laser pulse is shorter than electron-photon coupling time (tipically $1 - 100\,\text{ps}$) most of the energy is absorbed by the electrons. The thermal equilibrium of the electronic distribution is reached after the laser radiation, in a time that goes from a few hundreds of femtosecond to some picoseconds. In this way, a ultrafast laser can cause a heating of the electrons and generates a gas of hot electrons in equilibrium with each other but far from equilibrium with the lattice. Consequently, only a small fraction of the laser pulse energy is trasmitted to the lattice trough thermal diffusion and so the HAZ (heat-affected zone) is greatly limited [2] like shown in figure 1.1. Thanks to this feature it is possible to use ultrafast lasers to induce in the materials non-thermal effects that allow to realize high precision micromachining.

1.1 Non-linear effects.

Focusing the energy in a short time and in a small volume can lead to an intensity high enough to trigger in the irradiated material non linear phe-

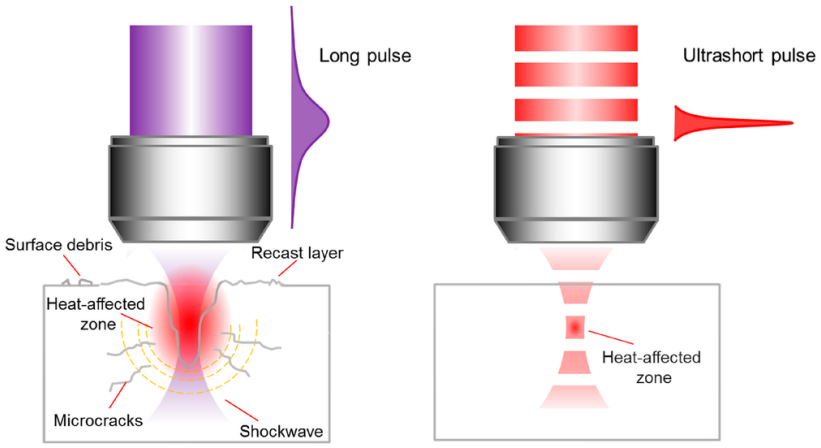

Figure 1.1: Difference between long and fast pulses interaction from [3].

nomena such as multiphoton absorption, avalanche ionization and absorbing plasma formation. These effects are very important because they allow to have interaction in systems which are forbidden with traditional sources.

1.1.1 MPI and tunnel ionization.

In the linear absorption an electron is excited from the valence band to the conduction band due to absorption of a photon with energy, $h\nu$, equal or greater than energy gap E_g of the material. If the photon has an energy lower than the energy gap the electron cannot jump from valence to conduction band. However, when a high density of photons impacts on the material, an electron can be promoted in conduction band by absorbing more than one photon, although each of these has an energy less than E_g. This phenomenon is known as multi-photon ionization (MPI). A ultrafast laser can easily lead to multi-photon absorption because it generates extremely high power peaks. This means that we can induce absorption even in materials that are transparent to the wavelength of the used source.

The numbers of photons m required to have ionization shall be such that:

$$mh\nu > E_g \tag{1.1}$$

where ν is the frequency of the incident light. The MPI probability strongly depend on how many photons arrive on the material per unit of area and time, in other words on the intensity of the laser source $I(r,t)$.

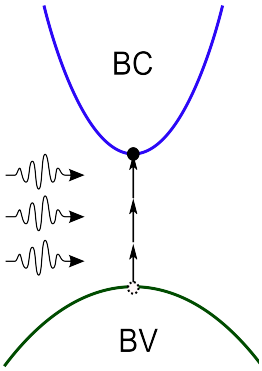

Figure 1.2: Multi-photon absorption scheme.

Specifically, the rate of absorption is:

$$\frac{\sigma_m}{mh\nu} I(r,t)^m \tag{1.2}$$

where σ_m is the m-photons absorption cross section.

Another phenomenon linked to the multi-photon absorption is the tunnel ionization that is the dominant process in regimes of high intensity and low frequencies. The strong electromagnetic field of the photon, in these cases, distorts the band structure of the material and reduces the potential barrier between the valence and the conduction band. Therefore, there may be transitions between the two bands due to the tunnel effect of the electrons through this reduced potential barrier.

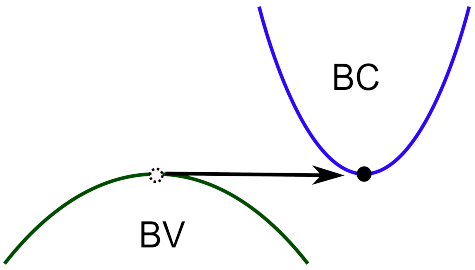

Figure 1.3: Tunnel ionization scheme.

These two phenomena can be explained with the same theoretical model, by using the Keldysh parameter γ [4]. The ionization probability is inversly proportional to the time $\tau_{tunneling}$ defined like:

$$\begin{aligned} \tau_{tunneling} &= \frac{\sqrt{m_e c n_0 \epsilon_0 E_g}}{eI} \\ \gamma &= \tau_{tunneling} \cdot \omega \end{aligned} \tag{1.3}$$

where m_e is the electron mass, e the electron charge, c speed of light, n_0 the refractive index of the material and ϵ_0 the permittivity of vacuum. The ω parameter is the frequency of the electric field. If $\gamma > 1.5$ multi-photons absorption is the main effect, while if $\gamma << 1$ tunnel ionization is the dominant effect. An example of free carrier evolution as a function of time is shown in figure 1.4.

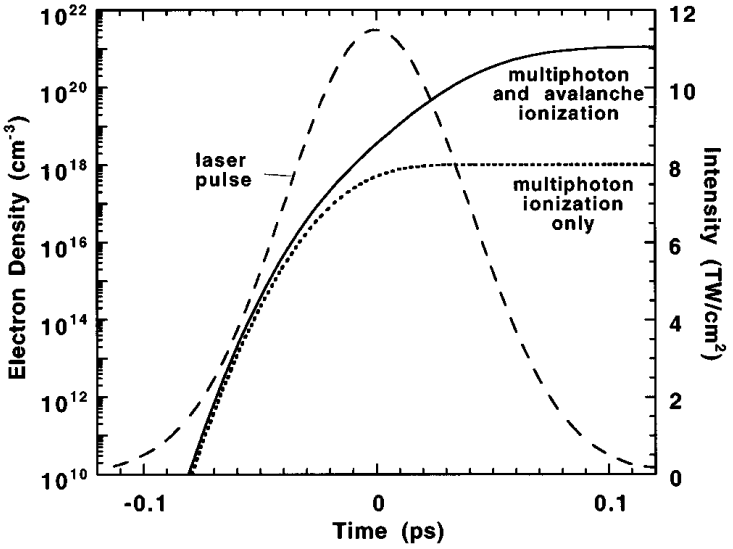

Figure 1.4: Example of free carrier evolution during the pulse time (100 fs pulse at 1053nm) in fused silica from [5].

1.1.2 Avalanche ionization.

An electron in the conduction band can still absorb energy from incident photons and move onto states with higher energy (Free Carrier Absorption). If an electron has an energy that exceeds the minimum of the conduction band of more than the energy gap, it can ionize another electron which is located on the maxiumum of the valence band through impact ionization. In this way there are two excited electrons at the minimum of the conduction band. These two electrons can still absorb energy and lead to an avalanche

process. The process is repeated until the laser electromagnetic field is strong enough to provide the necessary energy.

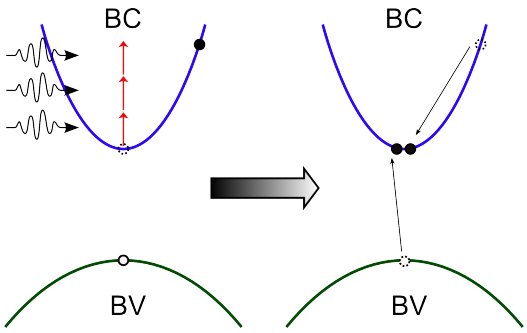

Figure 1.5: Avalanche ionization scheme.

This type of ionization needs a sufficient number of seed electrons in the conduction band to trigger the process. The seed electrons may be provided by thermally excited impurities or defects or, directly, from other non-linear effects of ionization. Therefore the probability of transition due to this process depend on the density of free carriers. For ultrafast laser pulses, as already said, the absorption occurs on a time scale shorter than the one needed to transfer the energy from electrons to the lattice. In this way the processes of absorption by the electrons and the heating of lattice are decoupled. The density of electrons grows in the conduction band due to avalanche ionization as long as the frequency of electrons plasma is equal to the laser frequency and then the plasma becomes strongly absorbent.

1.1.3 Recombination processes.

Once an electron is in the conduction band, it can fall back into the valence band through the recombination processes. There are various processes that lead to the recombination of electrons and holes and the probability that each of them occurs depends on the characteristics of the materials. In direct gap materials the probability of a radiative recombination (via photon emission, figure 1.6) is greater than in indirect gap materials, where the photon emission requires the presence of a phonon. The rate of emission is proportional to the product of electron density in the conduction band n and the hole density in the valance band p.

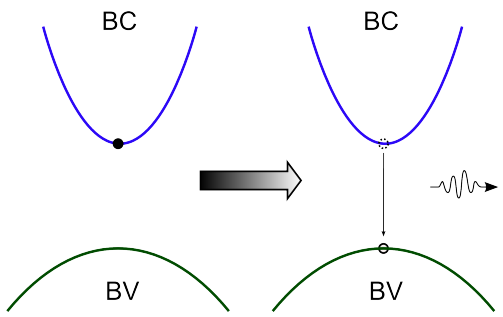

Figure 1.6: Photon emission.

In materials with many defects or impurities the recombination by deep impurity becomes relevant, figure 1.7, in which electron and hole recombine because of the presence of a trap state given by a defect. The recombination rate, in this case, depends also on the probability that the charges are captured by the trap state.

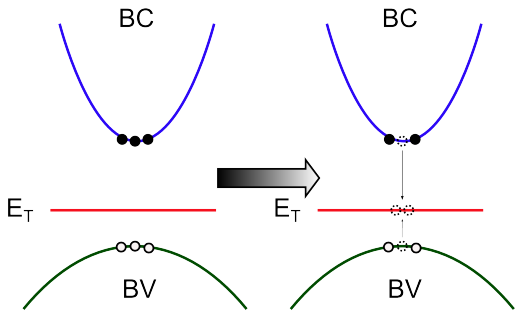

Figure 1.7: Deep impurity recombination.

In the case of high carrier injection, the most probable process is the Auger recombination, figure 1.8, in which an electron and a hole recombine in an interband transition and the excess energy is transferred to another free carrier.

Generally, all these processes act together and the total recombination has a characteristic time τ given by:

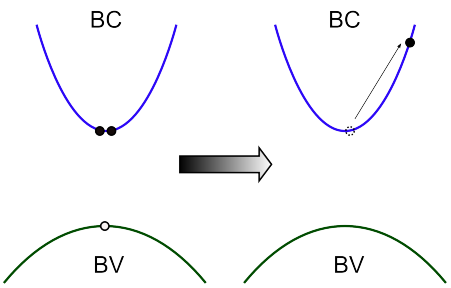

Figure 1.8: Auger recombination.

$$\tau = \left(\frac{1}{\tau_{emission}} + \frac{1}{\tau_{impurity}} + \frac{1}{\tau_{Auger}} \right)^{-1} \tag{1.4}$$

1.2 Beam propagation.

To study the beam propagation it is necessary to consider that the electromagnetic field of the beam within the irradiated material must satisfy the wave equation:

$$\nabla^2 u(\bar{r}, t) - \frac{1}{c^2} \frac{\partial^2 u}{\partial t^2} = 0 \tag{1.5}$$

where $u(\bar{r}, t)$ is the wave function that describes the electromagnetic field of the beam. For monochromatic waves with frequency ν, is often used the complex notation in which the beam is described by:

$$U(\bar{r}, t) = U(\bar{r}) \cdot e^{i2\pi\nu t} \tag{1.6}$$

called complex wave function.

In this approximation, the wave equation 1.5 is reduced to the Helmoltz equation:

$$\nabla^2 U(\bar{r}) + k^2 U(\bar{r}) = 0 \tag{1.7}$$

where k is the wave number.

As already said, the interaction with ultrafast light is characterized by nonlinear absorption phenomena that lead to the formation of a hot electrons plasma. The plasma changes the optical properties in the material and this

phenomenon can be described [6] by a complex dielectric function $\tilde{\epsilon}$.
The wave number k within the irradiated material is given by:

$$k = k_0 \cdot n = \frac{\omega}{c_0}\sqrt{\tilde{\epsilon}} \tag{1.8}$$

where ω is the pulsation of the beam and c_0 is the speed of light in vacuum. A generic solution of the equation 1.7 is:

$$\begin{aligned} U(\bar{r}) &= A(\bar{r}) \exp(ikz) \\ &= A(\bar{r}) \exp(i\mathrm{Re}[k]z) \exp(-\mathrm{Im}[k]z) \end{aligned} \tag{1.9}$$

Since the intensity $I(z,t)$ is proportional to the square modulus of $U(\bar{r})$, if $\mathrm{Im}[k] \neq 0$ the intensity decrease exponentially compared to the crossed thickness of material with absorption coefficient of $\alpha = 2\mathrm{Im}[k]$:

$$I(z,t) = I_0 \exp(-\alpha z) \tag{1.10}$$

The absorption coefficient α depends on the processes that take place during the light-matter interaction: linear absorption, multi-photon and FCA [7]. The variation of the intensity as a function of the thickness of the crossed material is given by:

$$\frac{\partial I(z,t)}{\partial z} = -\left[\left(\alpha_0 + \sigma_m I(z,t)^{m-1}\right)\frac{n_a}{n_a + n_i} + \alpha_{FCA}(z,t)\right] I(z,t) \tag{1.11}$$

where α_0 is the linear absorption coefficient, σ_m the cross section of m-photons absorption and α_{FCA} absorption coefficient of free carriers. The term $\frac{n_a}{n_a+n_i}$ represent the fraction of neutral atoms (n_a) to total (neutral and ionized), i.e. the atoms that can contribute to the absorption by the promotion of an electron from the valence band to the conduction band.

1.3 Applications.

The features of ultrafast pulses allow to have a high quality processing of many materials such as semiconductors and insulators or biological tissues where it is important to have a limited heat diffusion area to not damage the sorrounding tissues. This decrease in the HAZ also increases the spatial resolution of the process that can get down to the nanoscale. Intensity close to the ablation threshold lead to formation of nanostructures that have a periodicity much shorter than the used wavelength, figure 1.9.

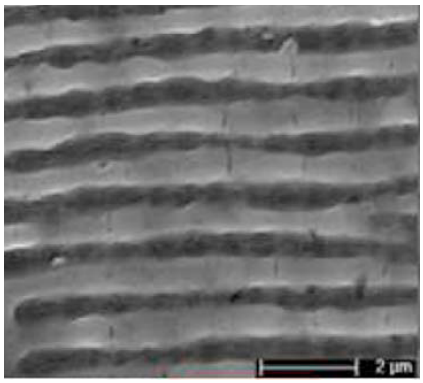

Figure 1.9: SEM image of nanoripples on ZnO crystal after irradiation with femtosecond laser [8].

Another important aspect is the presence of the nonlinear absorbition (like multiphoton absorption) that allows to modify the surface of materials (micromachining, drilling or cutting, figure 1.10) and also to have three-dimensional internal microfabrication in different types of materials, for example glass. The interaction can be spatially controlled thanks to a good beam focusing restricted to the area of interest.

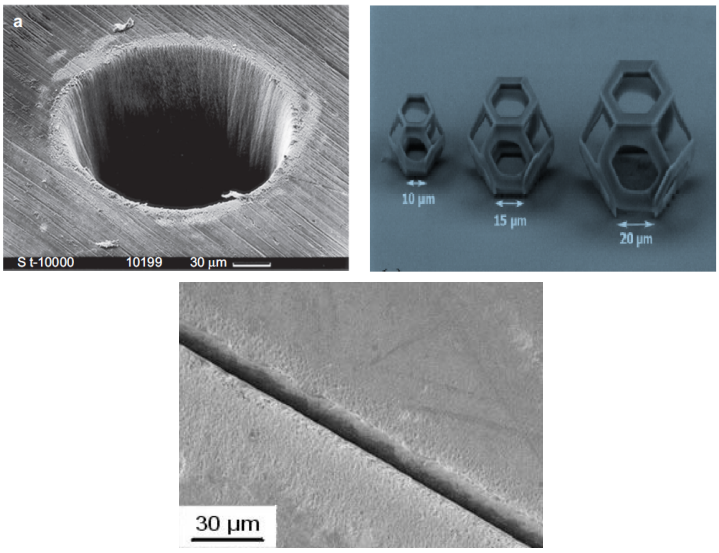

Figure 1.10: 3D machining of different dimension on polymer [9] (on right), hole on steel plate with a 200 fs laser (on left) [10]and a cut on a thin silicon plate made with a femtosecond laser (on bottom) [11].

Chapter 2

Photovoltaic industry.

An area where ultrafast laser sources can give new business solution is the photovoltaic industry. During the production of a photovoltaic silicon cell there are some processes that concerns the ablation of material, such as the opening of the dielectric passivating layers and the edge isolation [12]. These processes can find alternative solutions by micromachining techniques with laser technologies [13]. The benefits of these solutions consist mainly in the speed of the process, in a less thermal damage of the cell, in the maching precision, which can be summarized in a higher efficiency of the final device.

2.1 Solar cells.

A solar cell is a device that produces electricity from the solar light. To get electric power production it is necessary to satisfy two conditions: a material that absorbs solar light is required to have internal photogeneration of free carriers and to convey these carriers on an external circuit to produce both current and voltage.
A large variety of materials can satisfy these conditions, but, in pratice, almost all devices of this type take advantage of the properties of semiconductor materials (in most of the cases silicon) by using pn junctions.
The pn junctions are formed by two semiconductors materials in contact with each other, of which one is n-type doped and the other one p-type. Since the two materials touch each other, charges in excess in the two areas spread in the opposite area. In this way, in the p-type area negative ions that are fixed in the lattice remain uncovered and can not spread. Similarly, in the n-type positive ions remain uncovered. These ions form two layers of uncompensated charge, which creates a strong internal electric field localized at the interface between the two semiconductor materials. This region, called 'de-

pletion zone', is free from carriers thanks to the internal field and constitutes the active part of the junction. We have, therefore, different processes: the generation of carriers, diffusion, drift due to the electric field and recombination. All these processes at the equilibrium compensate each other.
In the case of the photovoltaic cells, in the majority of configuration the n-type area is much more smaller than the p-type area and, in this way, it is constituted by only the depletion zone. With this kind of structure, the only diffusion zone is the electrons diffusion zone (L_e), as shown in figure 2.1.

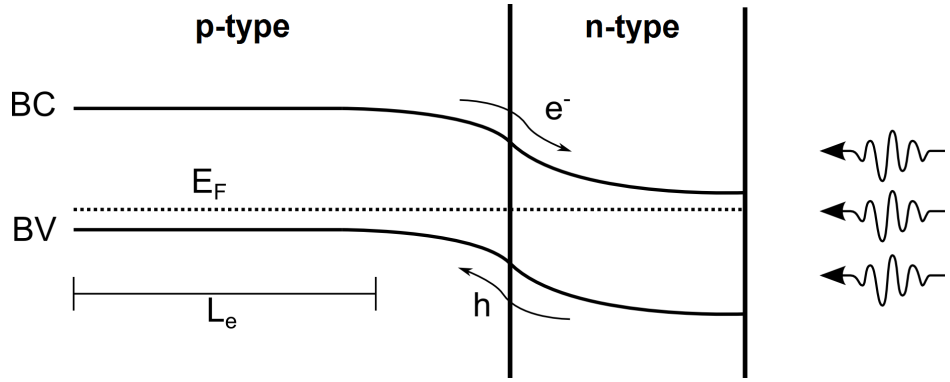

Figure 2.1: Band structure for a photovoltaics cell.

When a light wave of the appropriate frequency cross the depletion zone, electron-hole pairs are created within the material. The newly created charges are separeted from the inner field (collection of the free carriers). In this way, the generated charges recombine through the external circuit and you will measure the short-circuit current J_{SC}.
To produce electrical power it is necessary to have both a current and a voltage. If the free carriers are prevented from leaving the cell you will get an increase in the number of electrons in the n-type material and holes in the p-type due to the internal field. In this way, a potential V is produced by the charge accumulation. This potential results in another electric field opposite to the first (direct bias conditions). The total electric field is the sum of the two. In this condition, at the equilibrium a constant potential difference across the cell is obtained.
A good model to describe the operation of a photovoltaic cell is the model based on the Shockley relationship for an ideal pn junction in direct bias conditions, in which the current generated is given by:

$$J_{\mathrm{cell}} = J_0 \left(e^{\frac{eV}{KT}} - 1 \right) - J_{\mathrm{SC}} \tag{2.1}$$

where J_0 is called generation current and it is the current that would occurs across the junction if it is not illuminated.
Equation 2.1 expresses the current generated as a function of the potential V of the junction under illumination. The junction behaves as a generator of electric power, i.e. as a photovoltaic cell, in the case where $V > 0$ e $I < 0$. The first condition implies that the potential V is opposite to the internal potential in order to have the direct bias conditions, while the second one comes from the convention on the sign of the current in the circuit.

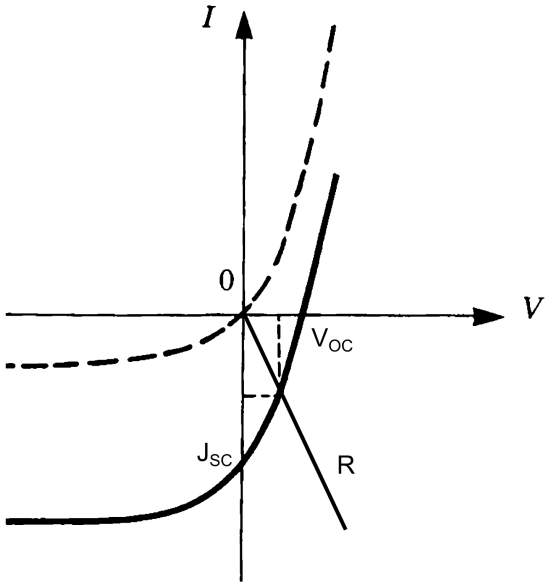

Figure 2.2: Produced current VS voltage.

The maximum extractable power $P_{\max}$ is given by the area of the rectangle in figure 2.2 and it depends on the load R given to the cell. If the cell is an ideal cell the extractable power would be $V_{\mathrm{OC}} \cdot J_{\mathrm{SC}}$, where V_{OC} is the open circuit voltage. The ratio between the maximum power and the ideal power divided by the surface of the cell S is called 'filling factor':

$$F.F. = \frac{P_{\max}/S}{J_{\mathrm{SC}} \cdot V_{\mathrm{OC}}} \tag{2.2}$$

The efficiency of the cell can be expressed as:

$$\eta = \frac{J_{\mathrm{SC}} \cdot V_{\mathrm{OC}}}{\Pi_0} \cdot F.F. \tag{2.3}$$

where Π_0 is the intensity of incident light on the cell.

2.2 PERC solar cell.

The objective of photovoltaic industry has been, over the years, to produce increasingly efficient devices trying, at the same time, to have low production costs to make this technology a competitive source of electricity. To achieve this purpose, different types of solar cells have been developed. For example, to lower the cost of production the thickness of the cell is decreased more and more (thin cell [14]). There are multi-junction cells that are formed by layers of different materials, each of them absorbs a region of the solar spectrum to obtain an overall very high absorption and thus a high efficiency. Having to use more materials the production cost of this type of cells is higher than the typical mono or multi-crystalline silicon cells which are more common. The PERC (Passivated Emitter and Rear Cell) cells are located in this last scenario. The rear side of PERC cell incorporates a passivation layer that is interrupted by small-area local aluminum contacts. In 1989, Blakers et al. have shown that it was possible to reach an efficiency of 22.8% with a cell of this type [15].

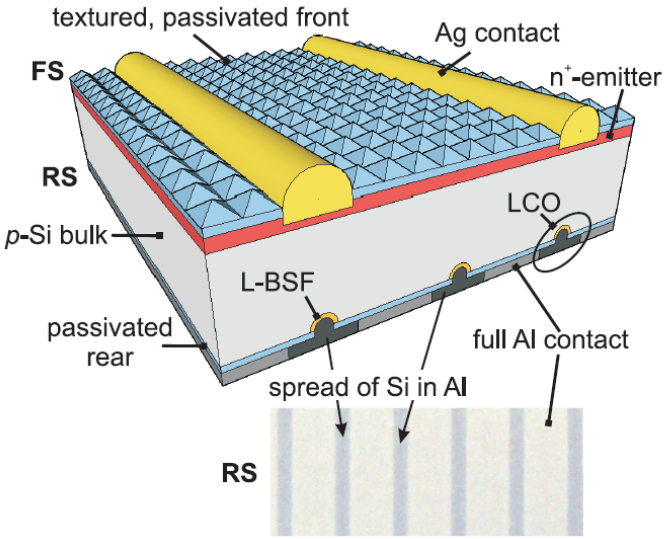

Figure 2.3: Structure of a PERC cell.

Figure 2.3 show a structure diagram of a PERC cell. The surface of the emitter is processed by acids in order to facilitate the internal reflections (texturing) and then placed in contact with an anti-reflective coating onto which the silver contacts are deposed. Smilar steps are done on the lower surface where one or more dielectric layers are placed in contact with the

silicon in order to have passivation. In this case, the passivation is processed with laser sources in order to depose the aluminum contacts.
The passivation is very important for two main reasons:the internal reflections of light within the cell are increased compared to cells which don't have the passivation and the recombination speed on the surface is reduced since the area affected by metallization with aluminum is reduced. As a consequence, the open circuit voltage increases by reducing the recombination at the rear side. The effect results in an increase of the average lifetime of the carriers within the junction and therefore to a greater efficiency of the final device. In this kind of cell a particular attention is needed to open the contacts. In non passivated cells, the back side is completely covered by aluminium.The cell is brought, therefore, at high temperatures (firing) and, in this way, part of the aluminum is incorporated by the silicon (alloy formation). The formation of this Al-Si alloy produced a thin electric field, that was named the Back Surface Field (BSF) by Mandelkorn et al. [16].

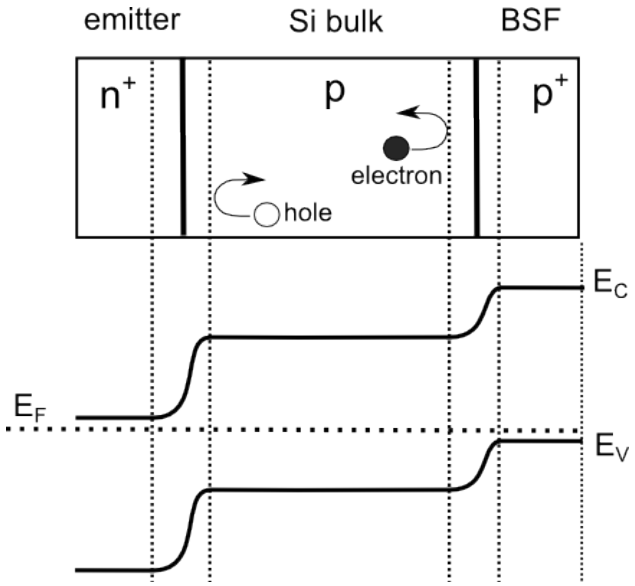

Figure 2.4: Effect of back surface field.

As shown in figure 2.4, the presence of the Al-BSF produce a heavily doped surface (p^+) between the silicon and the metal contact. The holes are injected at the end of the p-bulk and the electrons are driven back to the front, doing so reduce the surface recombination velocity. In this way, the solar cell has a lower resistivity of the silicon [17] and a higher V_{OC} under illumination [18], due to the increase of the majority carriers at the front of the silicon bulk.

However, in a PERC cell contacts are obviously local since the back side of the cell is passivated. Therefore is very important to find out the right balance between how much to decrease the effect of passivation while ensuring a good signal collection. Furthermore, it was demonstrated [19] that local contacts favor formation of the Al-Si alloy by increasing the performance of collection (Local BSF).

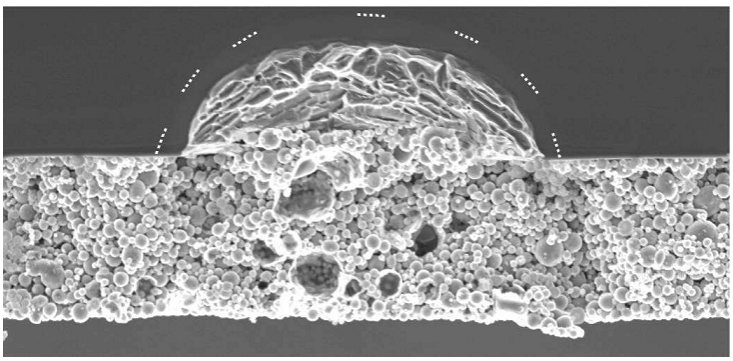

Figure 2.5: Rear side local contact [19].

2.3 Ultrafast machining on PERC cells.

The steps of production for a photovoltaic cell depend on the structure of the cell itself. For a PERC cell the production sequence is shown in figure 2.6.

The front surface is textured to increase light reflections. Afterwards, the surface is cleaned and a phosphorous diffusion is performed to create the emitter. After removing the phosphorous silicate glass from the surface and cleaning, the surfaces are covered by an antireflection coating on the front side and by a passivation layer on back side. Afterwards, the contacts are printed.

In this thesis, we focused our study on the opening of the passivating layers for the contact on the cell back side. Through interaction with ultrafast pulses it is possible to do a very precise work and minimally invasive. The objective of this work is to open the contacts in the thin dielectric layer (average thickness approximately 100 nm) with the least possible damage to the underlying silicon and surrounding passivated areas.

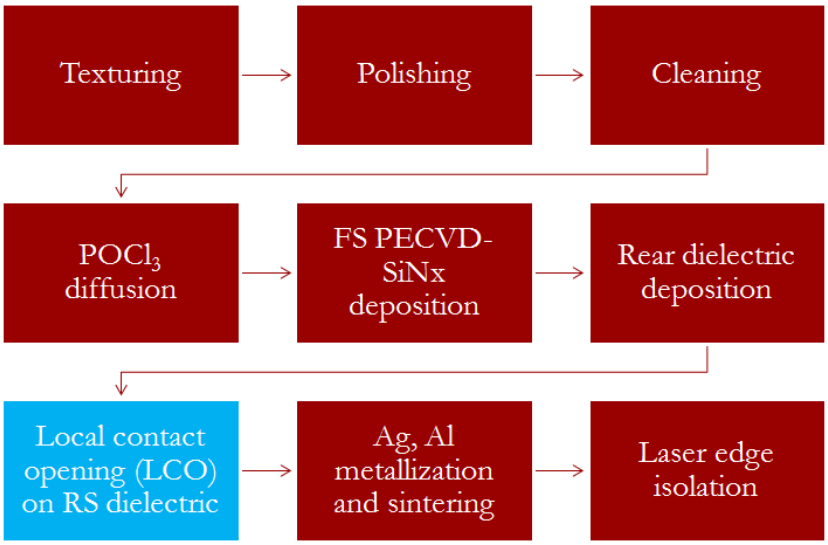

Figure 2.6: Production sequence for a PERC cell.

Chapter 3

Lift-off process.

Our objective is to study a process that is localized and precise for opening the back side dielectric layers of the cells in order to print the aluminum contacts. To minimize damage on the structure it is necessary to remove the material in the affected areas by evaporation through the interaction with the laser light. This process is called ablation: in a localized area the material absorbs energy to bring it from solid state directly to the gaseous state. The ablation is realizable with different laser sources (for example nanosecond laser in the UV regime) but it leads to thermal processes due to heat conduction [21]. These effects, as already said, are minimized using ultrafast laser pulses and in particular in the femtosecond regime.

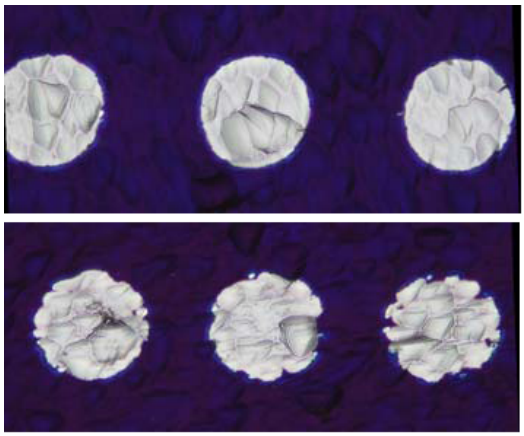

Figure 3.1: Ablation with UV laser pulses of 400 fs (top) and 10 ps (bottom) from [22]

Another ablation technique studied is the 'lift off' process [23]. It is a

process of indirect ablation: the dielectric is transparent to the laser wavelength, and then most of the intensity is absorbed by the silicon substrate which evaporates and causes the delamination of the dielectric layer due to the pressure produced. The layer of silicon that evaporates is very thin, of the order of few tens of nanometers or less [24].
This process has a strong dependence by the laser beam parameters and by the physical and chemical characteristic of the passivation material, but, generally, it has lower interactions thresholds than direct ablation and it is less affected by thermal effects. Specifically, it is possible to identify three different regimes depending on the used fluence Φ [J/cm^2] [25]:

- at low fluences, figure 3.2, there is a change in the material reflectivity (and thus a color change). The minimum fluence at which this phenomemon is observed is called melting threshold fluence $\Phi_{\mathrm{th,m}}$. Under these conditions the silicon substrate has absorbed enough energy to melt and then recrystallize without other damages.

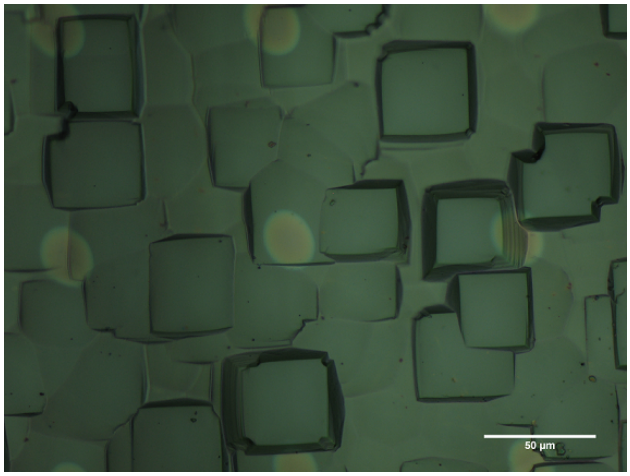

Figure 3.2: Low fluences. Sample processed with $\lambda = 1028\,\mathrm{nm}$, focal lens 200 mm and repetition rate 500 kHz.

- the minimum fluence required for delamination is $\Phi_{\mathrm{th,b}}$ (breaking threshold fluence). This regime concerns the mechanical part of the process: the silicon substrate has absorbed enough energy to evaporate and raise the dielectric layers (it creates a kind of steam bubble) until it breaks exposing the underlying silicon, figure 3.3.

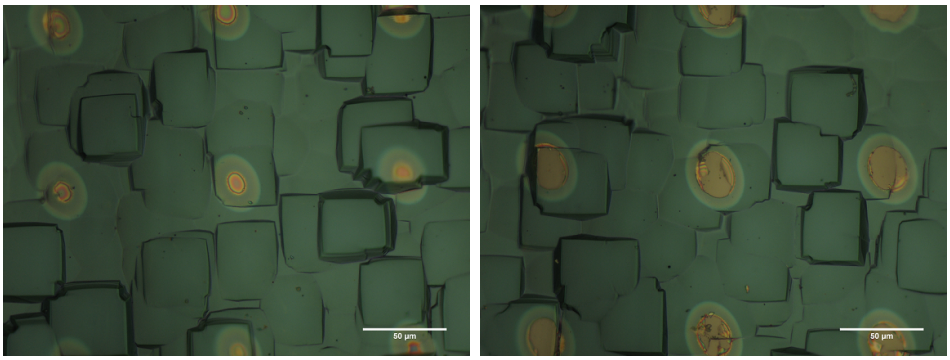

Figure 3.3: Breaking threshold fluence. It can clearly be seen on the left the raised dielectric bubble, on the right the underlying silicon. Samples processed with $\lambda = 1028\,\text{nm}$, focal lens 200 mm and repetition rate 500 kHz.

- finally, if the fluence is too high, the energy will be absorbed directly by the dielectric layers due to the nonlinear absorption. The pulses, in this way, interact directly with the dielectric but without damaging it. In order to have direct ablation of the dielectric, even higher fluences are necessary. In this regime we will observe an 'island' of insulating material at the center of the spot, as shown in figure 3.4. The minimum fluence for this phenomenon is $\Phi_{\text{th,i}}$ (island threshold fluence).

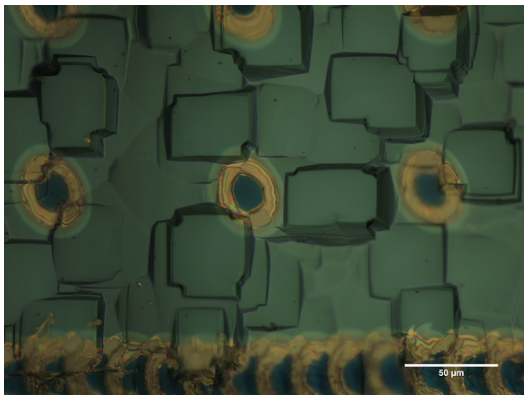

Figure 3.4: Island threshold fluence. Sample processed with $\lambda = 1028\,\text{nm}$, focal lens 200 mm and repetition rate 500 kHz.

If the laser beam is well described by the Gaussian formalism, its intensity is a function of ρ, the radius of the beam in the plane perpendicular to the

propagation direction, and of z, the position on the propagation axis. This function is:

$$I(\rho, z) = I_0 \left[\frac{\omega_0}{\omega(z)}\right]^2 \exp\left[-\frac{2\rho^2}{\omega^2(z)}\right] \tag{3.1}$$

where $\omega(z)$ is the waist of the beam (defined as the radius at which the intensity is equal to $1/e^2$ of the maximum intensity) and ω_0 is the radius of the beam at the position $z = 0$. Since the maximum intensity is at the center of the spot, it is possible that the fluence in the central area of the spot exceeds the damage threshold $\Phi_{\text{th,i}}$, while in the outlying areas the fluence remain below this threshold. The result is shown in figure 3.4: in the central zone there is a dielectric island, all around is present a ring that is located in an intermediate regime between $\Phi_{\text{th,b}}$ and $\Phi_{\text{th,i}}$. Similarly, the last outer ring of lighter color will be above $\Phi_{\text{th,m}}$ but under $\Phi_{\text{th,b}}$.
In this case, there is not a complete delamination of the interested area therefore it is called 'partial lift-off'.

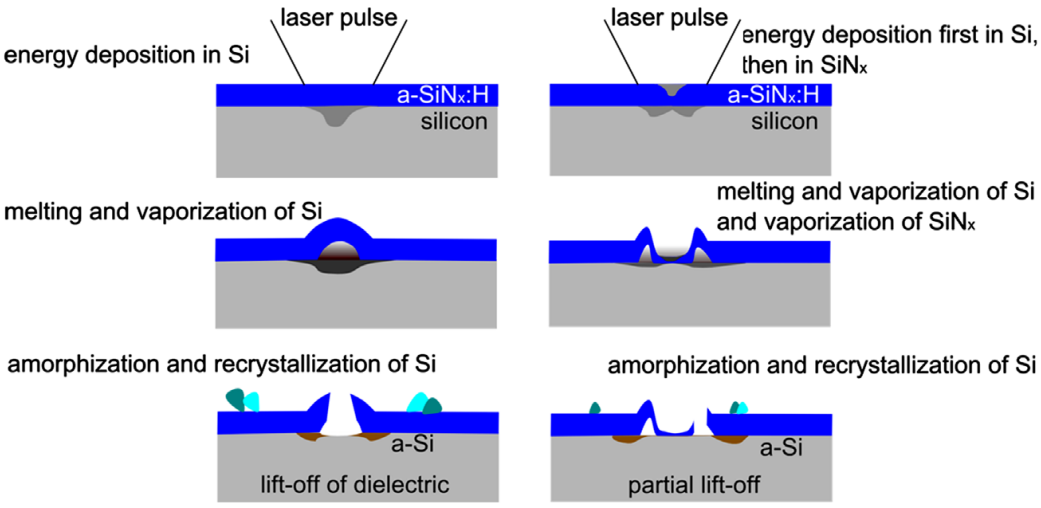

Figure 3.5: Comparison between total delamination(on the left) and partial (on the right), from [25].

Chapter 4

Experimental setup.

A block diagram of the experimental setup is shown in figure 4.1. The used source is a PHAROS laser system that is based on an ytterbium amplifier (Yb:KGW). The source produces a pulsed beam with a maximum power of 12 W, maximum pulse energy 1 mJ, repetition rate of pulses from 1 kHz to 1 MHz and pulse duration varying from 200 fs to about 10 ps.

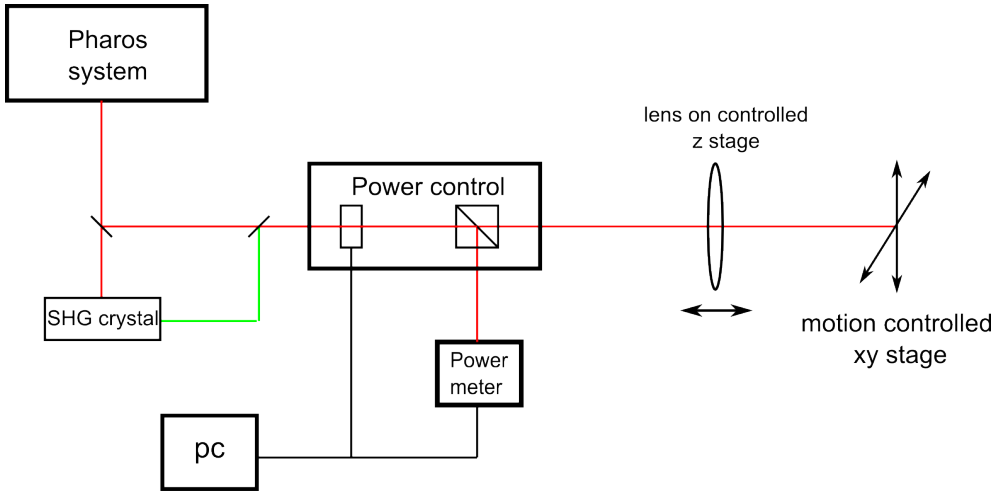

Figure 4.1: Experimental setup diagram.

At the output of the laser system, the beam is deflected by some mirrors to an attenuator (Altechna Watt Pilot) that it is used to control the beam power. At the end, a lens focuses the beam on the sample that is placed on a nanometric translator (Aerotech Nanometric XYZ stage) that allows to move the sample on the plane perpendicular to the beam direction and also to move the focusing lens on the optical axis. The translator is controlled by

software.

4.1 Power control.

Inside the attenuator, the beam passes through a $\lambda/2$ plate that can rotate on the plane perpendicular to the beam direction and through two polarizers set at Brewster angle. In this way, the beam is divided into two channels, as shown in figure 4.2: the transmitted channel with polarization p (the electric field of the light wave lies in the plane of incidence) and the reflected channel with polarization s (the field is perpendicular to the plane of incidence).
By turning the plate we can increase or decrease the light intensity in one channel or the other. By choosing the output of only one of two channels the attenuator can be used to control the beam power without changing the features of the source.

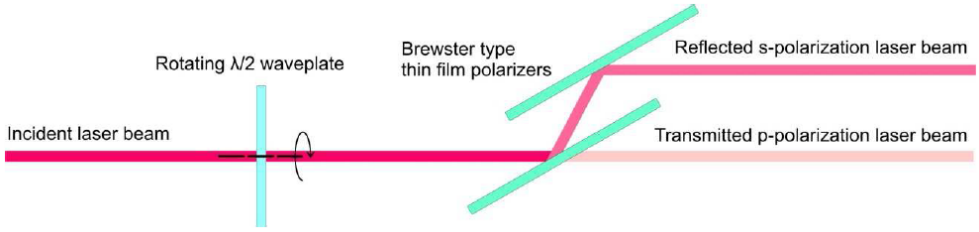

Figure 4.2: Watt Pilot diagram.

To express the light intensity after the attenuator as a function of plate rotation angle is sufficient to consider that rotating the plate of an angle θ produces a rotation of 2θ of the laser polarization plane. This happens because the rotation introduces a phase delay π in the field component that propagates along the extraordinary axis [26].
This effect is easily describable by the Jones matrices formalism [27]: (x, y, z) is the laboratory reference frame and (s, f, z) is the plate frame. The z axis is the propagation axis and it is the same for the two reference frames.

The Jones vector that describes the initial electric field of the beam in the plate frame is:

$$\begin{pmatrix} E_s \\ E_f \end{pmatrix} = R(\theta) \begin{pmatrix} E_x \\ E_y \end{pmatrix} \tag{4.1}$$

where $R(\theta)$ is the rotation matrix of angle θ that describes the angle between the two frames. After crossing the plate, the electric field direction

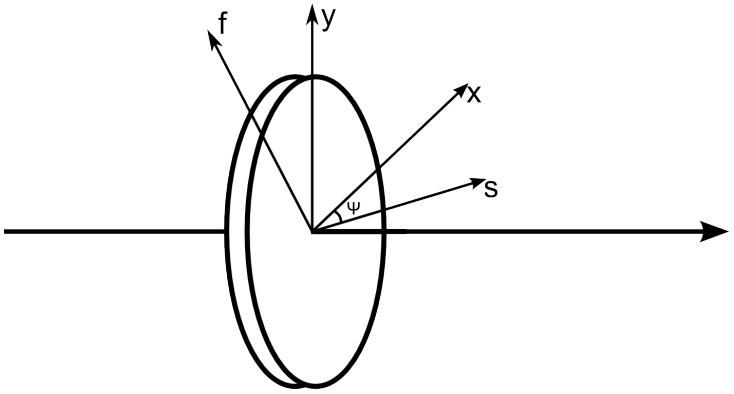

Figure 4.3: Comparison between the laboratory and plate frames.

is changed: the component that propagates along the s (slow) axis crosses the plate thickness d with a refractive index n_s while the component along the f (fast) axis crosses the same thickness d but with a refractive index n_f. The components of the field after the plate are given by:

$$\begin{pmatrix} E'_s \\ E'_f \end{pmatrix} = \begin{bmatrix} \exp\left(-in_s \frac{2\pi}{\lambda} d\right) & 0 \\ 0 & \exp\left(-in_f \frac{2\pi}{\lambda} d\right) \end{bmatrix} \begin{pmatrix} E_s \\ E_f \end{pmatrix} \tag{4.2}$$

You can define a phase delay Γ that depends on the difference between the refractive indices:

$$\Gamma = \frac{2\pi}{\lambda}(n_s - n_f)d \tag{4.3}$$

In the case of a $\lambda/2$ plate, it is equal to π. Similarly, you can define the overall average phase shift:

$$\phi = \frac{1}{2}(n_s + n_f)\frac{2\pi}{\lambda}d \tag{4.4}$$

by which the equation 4.5 becomes:

$$\begin{pmatrix} E'_s \\ E'_f \end{pmatrix} = e^{-i\phi} \begin{bmatrix} \exp\left(-i\frac{\Gamma}{2} d\right) & 0 \\ 0 & \exp\left(i\frac{\Gamma}{2} d\right) \end{bmatrix} \begin{pmatrix} E_s \\ E_f \end{pmatrix} \tag{4.5}$$

Therefore, in the case of a $\lambda/2$ plate the final electric field in the laboratory frame will be:

$$\begin{pmatrix} E'_x \\ E'_y \end{pmatrix} = e^{-i\phi}\,(-i\phi) \begin{bmatrix} \cos(\theta) & -\sin(\theta) \\ \sin(\theta) & \cos(\theta) \end{bmatrix} \begin{bmatrix} -i & 0 \\ 0 & i \end{bmatrix} \begin{bmatrix} \cos(\theta) & \sin(\theta) \\ -\sin(\theta) & \cos(\theta) \end{bmatrix} \begin{pmatrix} E_x \\ E_y \end{pmatrix}$$

that becomes

$$\begin{pmatrix} E'_x \\ E'_y \end{pmatrix} = e^{-i\phi} \begin{bmatrix} \cos(2\theta) & \sin(2\theta) \\ \sin(2\theta) & -\cos(2\theta) \end{bmatrix} \begin{pmatrix} E_x \\ E_y \end{pmatrix} \tag{4.6}$$

The light intensity is the squared modulus of the field and, so, after the attenuator it will be equal to $I = I_0 cos^2(2\theta)$ for the reflected channel and $I_0 - I$ for the transmitted channel where I_0 is the intensity of the laser output.

By turning the half-wave plate one full turn four complete oscillations of the squared cosine are observed.

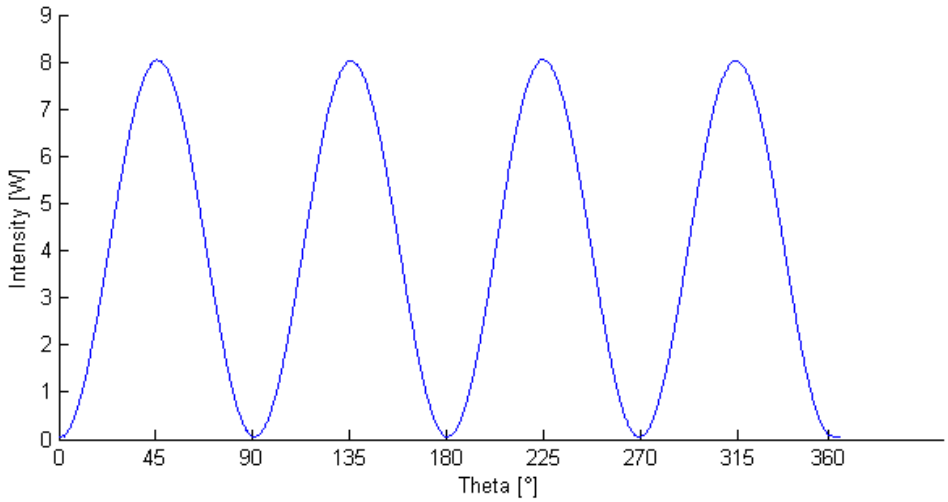

Figure 4.4: Intensity recorded after the attenuator.

The figure 4.4 shows the intensity, as a function of the rotation angle, recorded by a power meter placed after the attenuator where one of the two channels has been obscured. By fitting the experimental data with a function of the type:

$$I(\theta) = A \cdot cos^2(\theta + \phi_0) \tag{4.7}$$

we get the following parameters:

Amplitude	$A = (7.98 \pm 0.01)\, W$
Initial phase	$\phi_0 = (1.601 \pm 0.001)\, \text{rad}$

The trend of the experimental data is the expected one. By propagating the errors resulted from the fit, neglecting the error on the parameter ϕ_0, we

find that the error associated to the maximum of recorded intensity is just the error associated to the A parameter:

$$\sigma_{I\max} = \frac{\sigma_A}{A} \cdot I_{\max} = 0.01\, W \tag{4.8}$$

Therefore, we can assume to be able to control the power with a precision of the tens of mW.

4.2 FROG.

The used laser system allows to change the pulse time width thanks to the presence of a compressor. The compressors use angular dispersion optical materials which introduce a time-dependent frequency modulation (chirp). The pulse is decomposed into its spectral components which are phase shifted by different amounts and lastly all the components are reassembled together. The effect of the dispersion is greater for ultrashort pulses because they have larger spectral widths than long pulses.

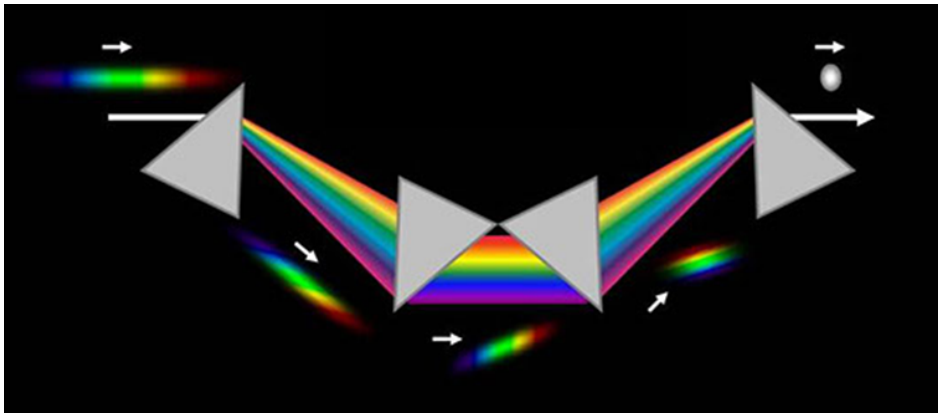

Figure 4.5: Compressor diagram [28].

The relationship between the temporal width of the pulse submitted to a chirp filter and the chirp parameter of the filter b is given by:

$$\tau_2 = \tau_1 \sqrt{1 + b^2/\tau_1^4} \tag{4.9}$$

where τ_1 is the time width of the transform limited pulse.
In order to associate each position of the compressor with the actual duration of the produced pulses a characterization is required. For this reason, we

assembled a system that uses the technique of Frequency Resolved Optical Grating (FROG), which is shown in figure 4.6.

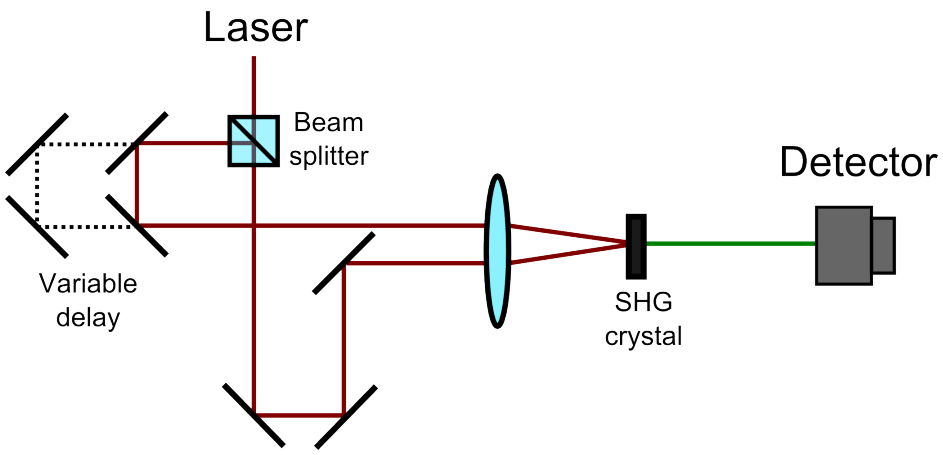

Figure 4.6: Block diagram of FROG.

In the realized system a laser pulse is divided into two components by a beamsplitter. One of the two components, $U(t-\tau)$, is delayed in respect to the other, $U(t)$, with a variable delay generated with a mirror placed on a nanometer shifter pilotable by software.
To select a window of the sum of two components we have exploited a SHG gate: the two pulses are focused into a nonlinear crystal that generates a second harmonic component only when the two pulses overlap, ie when the delay is comparable to the pulse duration. After removing the first harmonic components with a slit, the signal is sent to the spectrometer where the different spectral components are dispersed and analyzed.

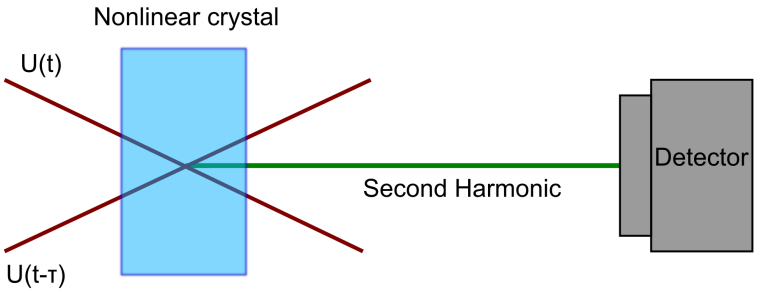

Figure 4.7: Second harmonic conversion.

From this analysis the spectrogram of the pulses $S(\nu, \tau)$ is obtained. The spectrogram represents the variation of the pulse spectrum in respect to the time and it can be written as:

$$\begin{aligned} S(\nu,\tau) &= |\Phi(\nu,\tau)|^2 \\ \Phi(\nu,\tau) &= \int U(t)U(t-\tau)\exp[-j2\pi\nu t]dt \end{aligned}$$

Since what is measured, $I_{FROG}(\nu,\tau) = |\Phi(\nu,\tau)|^2$, is the square modulus of the spectrum, the phase information is completely lost. For this reason an iterative numerical method is used since it allows to reconstruct this information. A signal which represents the electric field of the pulse is generated and then it is rewritten in the spectral domain by the Fourier transform to be compared with the actually measured signal. With a cyclic process the approximation of the real field with its phase is progressively improved.

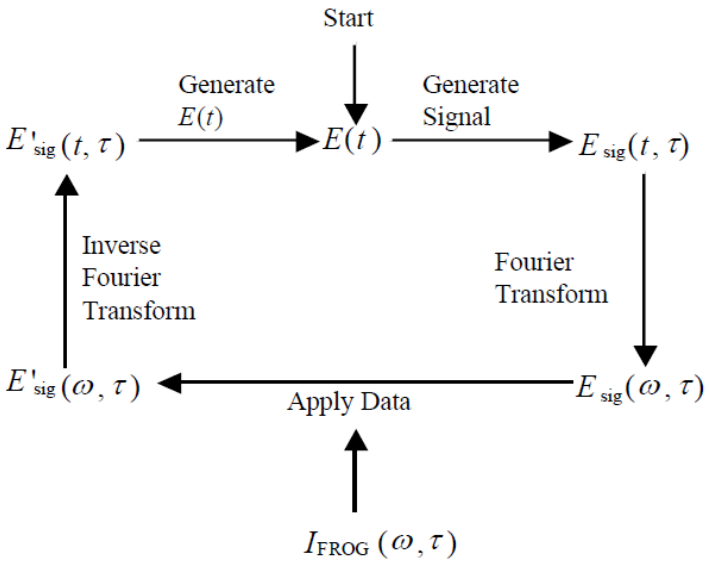

Figure 4.8: Diagram of the phase reconstruction algorithm [28].

By using the FROG analysis it is possible to associate each position of the compressor with the actual duration of the pulses like shown in figure 4.9.

The experimental trend is in agreement with the chirped optical pulse theory and described by the equation 4.9 reported in the figure as a solid blue line. The position of the transform limited pulse results to be 61000 steps.

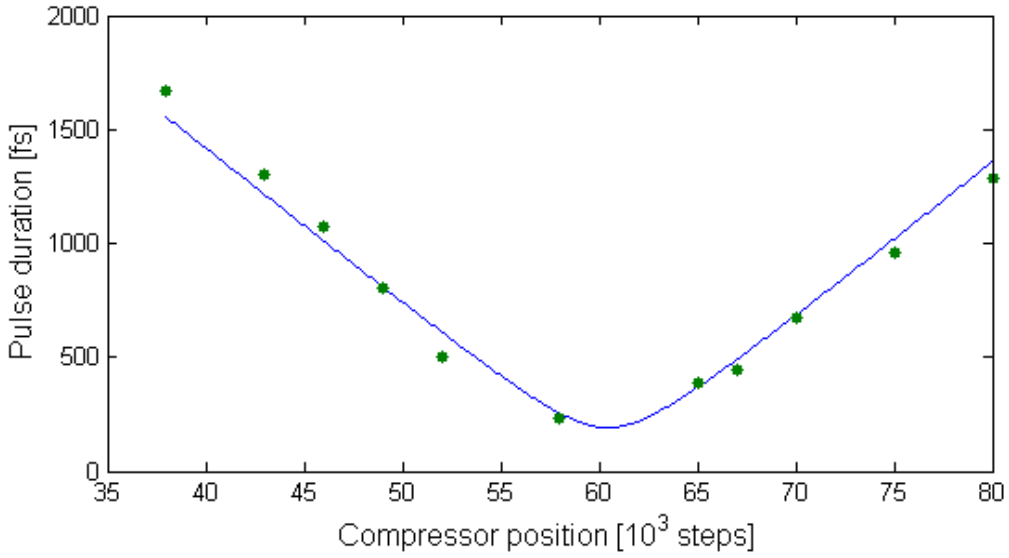

Figure 4.9: Pulse width as a function of the compressor engine position.

Chapter 5

Experimental measurements.

The objective of the study is to investigate the ablation process with ultrafast pulses on the basis of the caractheristics of the source and the material. The samples processed are 180 μm thick solar cells of texturized monocrystalline silicon which presents two layers of passivation dielectric material: the first layer of Al_2O_3 with a thickness less than 20 nm and the second of SiN_x with a thickness less than 90 nm.

5.1 Threshold fluence analysis

Since the phenomena under consideration are threshold phenomena, and so they do not appear below a certain value of absorbed energy, the material response to the interaction can be characterized by the threshold fluence above which you have indirect ablation and by the threshold fluence above which you have damage in the central area of the spot. These two fluences determine the window within which it is possible to have the indirect ablation process.
Assuming to use a perfect Gaussian beam, the fluence Φ is expressed as:

$$\Phi(\rho) = \Phi_0 \exp\left(-2 \cdot \frac{\rho^2}{\omega_0^2}\right) \tag{5.1}$$

$$\Phi_0 = \frac{2E_p}{\pi\omega_0^2} \tag{5.2}$$

where ρ is the beam radius on the plane perpendicular to the propagation direction, ω_0 is the beam waist (defined as the radius at which the intensity is equal to $1/e^2$ of the maximum intensity) and E_p is the pulse energy. Using this formalism, you can express the fluence threshold for any effect as:

$$\Phi_{\text{th}} = \Phi_0 \exp\left(-2 \cdot \frac{\rho_{\text{th}}^2}{\omega_0^2}\right) \tag{5.3}$$

In this way it is possible to relate the diameter D of the observable spot on the material with the fluence used for processing:

$$D_{\text{th}}^2 = 2\omega_0^2 \ln\left(\frac{\Phi_0}{\Phi_{th}}\right) \tag{5.4}$$

and, therefore, you can estimate the fluence threshold of the phenomenon by measuring the size of the delaminated areas.

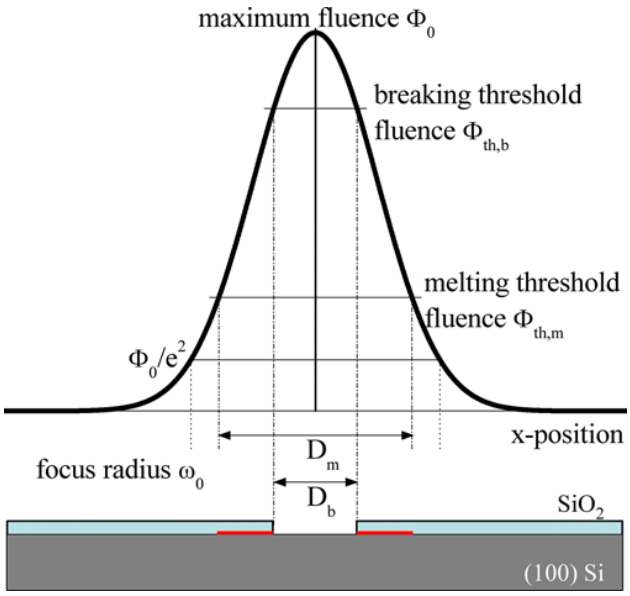

Figure 5.1: Gaussian profile and threshold fluences, by [24].

5.2 Femtosecond pulses.

In order to do this kind of analysis, the samples were processed according to the diagram shown in figure 5.2. For a given power a row is processed with a distance of 100 μm between one spot and the other. In this way, each row corresponds to a different power, increasing from top to bottom. The used parameters of the source are reported in table 5.1:

Wavelength	1028 nm
Average power	$0 - 10$ W
Repetition rate	500 kHz
Maximum pulse energy	20 μJ
Lens focal	200 mm

Table 5.1: Source parameters in femtosecond regime.

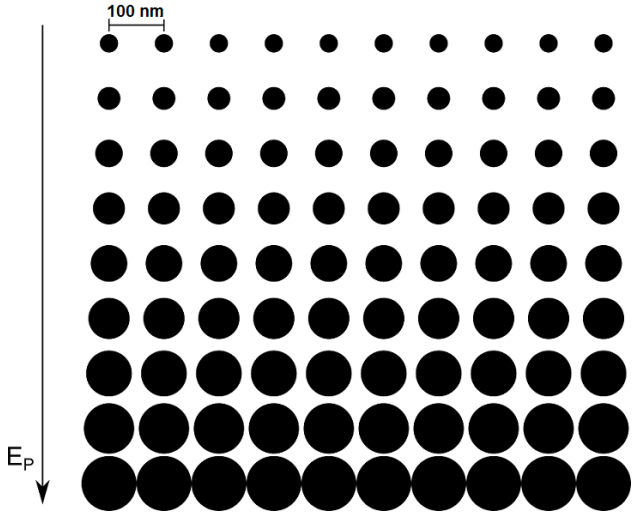

Figure 5.2: Scheme of a processed sample.

In figure 5.3 is shown the square of spots diameter for all the three phenomena (melting, breaking, island) as a function of the natural logarithm of the power used for each row. As a matter of fact, since the waist of the beam depends only on the focusing condition (for example, on the focal length of the lens used to focus), that do not vary while processing, there is a correspondence between the used power and the fluence. The equation 5.4 can be rewritten as a function of the power:

$$\begin{aligned} D_{\text{th}}^2 &= 2\omega_0^2 \ln\left(\frac{P}{P_{\text{th}}}\right) \\ &= 2\omega_0^2 \ln(P) - 2\omega \ln(P_{\text{th}}) \end{aligned} \tag{5.5}$$

From the fit of the reported data with the trend described by the equation 5.5, the angular coefficient of the linear interpolation that corresponds to the term $2\omega_0^2$ is obtained and also the intercept with the x axis that cor-

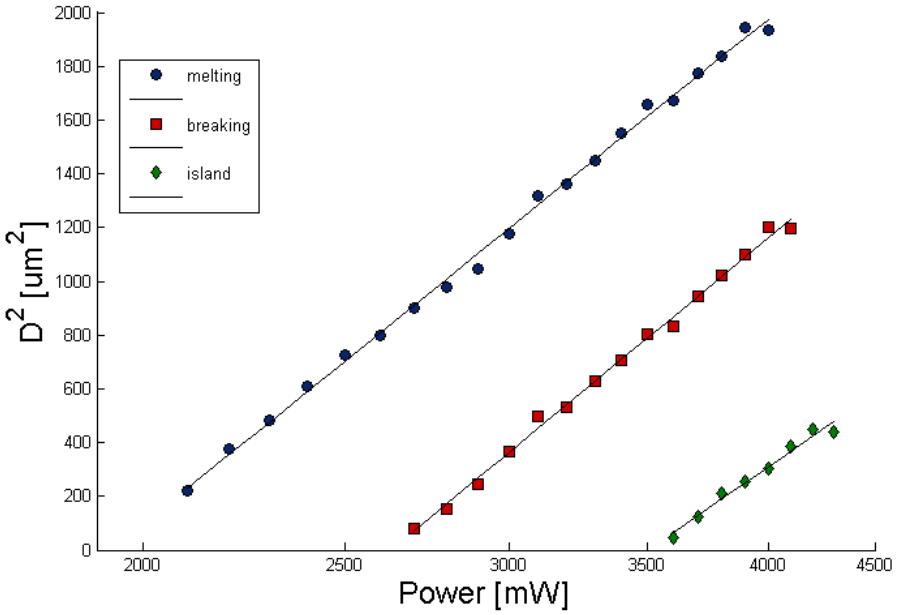

Figure 5.3: Analysis of the threshold fluences.The powers axis is in logarithmic scale.

responds to $\ln(P_{\text{th}})$ from which you get the threshold fluence:

$$\Phi_{\text{th}} = \frac{P_{\text{th}}}{\nu_{\text{rep}} \cdot \pi\omega_0^2} \tag{5.6}$$

where $\nu_{\text{rep}} = 500\,\text{kHz}$ is the repetition rate of the pulses.

In our case, we have analysed the samples with an electronic microscope and implemented a Matlab code that allows to do the analys just described.

From this analysis we found the threshold fluences for all the effects:

$$\begin{aligned}
\omega_0 &= (36.80 \pm 0.22)\,\mu\text{m} \\
\Phi_{\text{th,m}} &= (181.38 \pm 23.56)\,\text{mJ/cm}^2 \\
\Phi_{\text{th,b}} &= (241.50 \pm 47.13)\,\text{mJ/cm}^2 \\
\Phi_{\text{th,i}} &= (381.51 \pm 26.91)\,\text{mJ/cm}^2
\end{aligned}$$

These fluences are above the fluence needed to ablate silicon [29] with the laser parameters used by us. In particular, many studies [30] [31] [32] have

investigated the possibility that in this regime the silicon is heated close to its critical temperature and then it falls between the spinodal and binodal lines in a metastable zone.

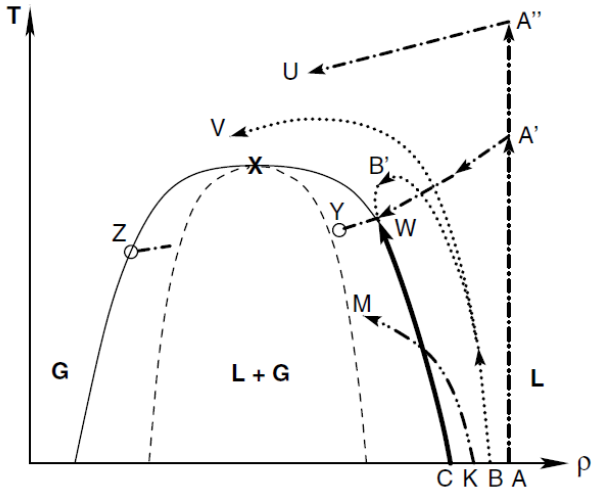

Figure 5.4: The graph shows the phase diagram for a semiconductor in the T-ρ section. The phases are labeled G for gas and L for liquid. The thin solid line is the binodal while the dashed line is the spinodal. Graph taken from [33].

In the first step after heating, the evaporated material develop a high pressure underneath the surface which generates a compressive shock wave. Most likely, the delamination is caused by the fenomenon of 'spallation' [34]: the front wave is reflected by the silicon surface after crossing the layer of oxide and then delaminate the passivation layer when the forces generated overcomes the strength of the interface.
With this type of analysis we can characterize the response of any material. The defects and small differences by which, in principle, a cell can be affected are negligible for this kind of analysis. As a matter of fact, by repeating the same measurments on different areas of the same cell there were not appreciable differences.

5.3 SEM and EDX analysis.

The Scanning Electron Microscope (SEM) is an electro-optical device used to obtain information on surfaces. An electron beam is controlled to scan

the area of interest. From the interaction between the electrons and the surface different phenomena take places, including the emission of secondary electrons and the re-emission or reflection of high energy electrons belonging to the primary beam. From the detection of these electrons a binary image of the sample surface is obtained. In addition to the electrons, after the interaction with the primary beam, photons are also emitted at different energies including X-ray. By recording the intensity of the produced X-ray and their distribution of energy, it is possible to have a chemical analysis of the elements present on the sample surface (EDX analysis).

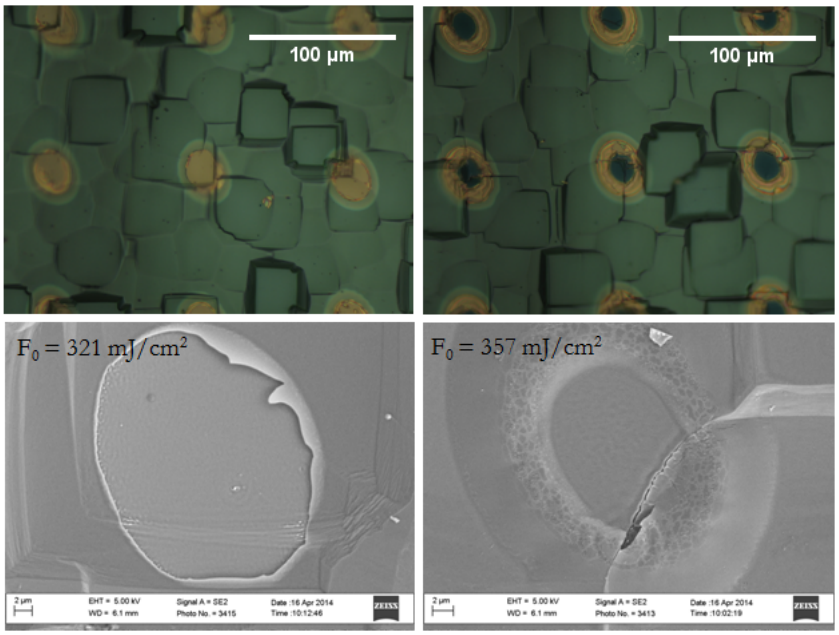

Figure 5.5: Delaminated spots (on left), spots with central dielectric island (on right) and respective SEM images.

Following is reported the analysis made in the different regimes of interaction with ultrafast pulses.

Breaking regime. Since the electron microscope operates through interaction of the beam of primary electrons with the sample, it is not possible, in this analysis, to study the first regime of low fluences of the delamination process. The 'melting' regime is, in fact, characterized by a difference in the refractive index of the area affected by the beam and, therefore, by a color change of the sample and it is, consequently, visible only with an optical microscope analysis but not with an electronic one.

However, for the 'breaking' regime it was analyzed an area of 10x10 μm both within the laser spot and externally in order to make a comparison.

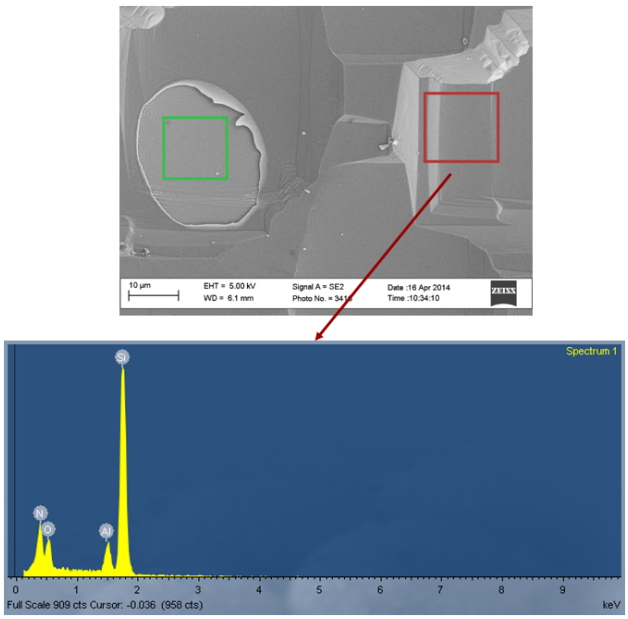

Figure 5.6: Elemental analysis of a non processed area.

Outside of the analyzed spot the analysis show the materials that constitute the two dielectric layers (Al, O, N) and silicon. Inside of the spot, instead, only the presence of silicon is clear. This result is in perfect agreement with the theory of the' lift-off '. The used fluence is sufficient to lead to the delamination of the passivation layer without exceeding the damage fluence. By increasing the fluence you can damage the silicon without interaction with the dielectric and, therefore, there is not the formation of the central island. This is observed in figure 5.8 where the inside of the delaminated spot is not clean, but shows signs of damage.

Island regime. For even more high fluences, as seen, the pulses begin to interact directly with the dielectric layers making impossible the indirect delamination. The elemental analysis 5.9 is in agreement with what was expected: in the center of the spot are still present the elements that constitute the passivation ie aluminum, oxygen and nitrogen in addition, obviously, to the silicon.

All analysis were performed with a Zeiss Supra 40VP electron microscope (voltage of the primary beam from 0.02 to 30 kV, 1.9 nm resolution @ 1 kV).

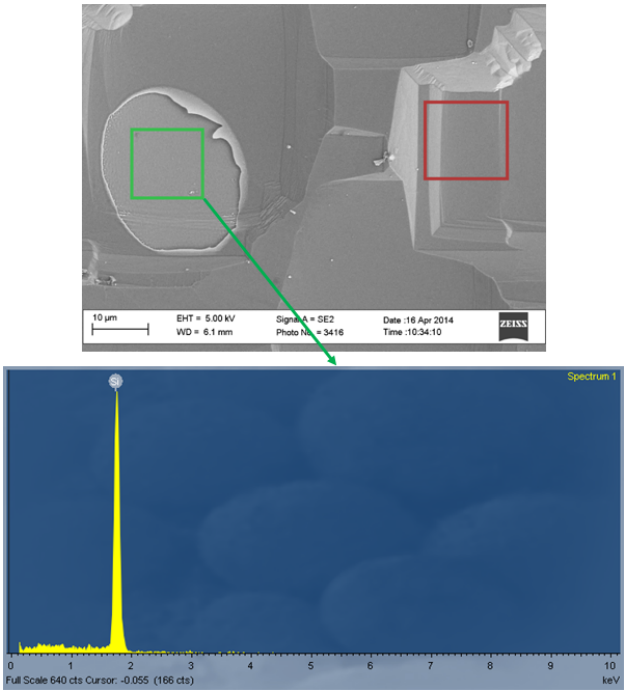

Figure 5.7: Elemental analysis of a delaminated area.

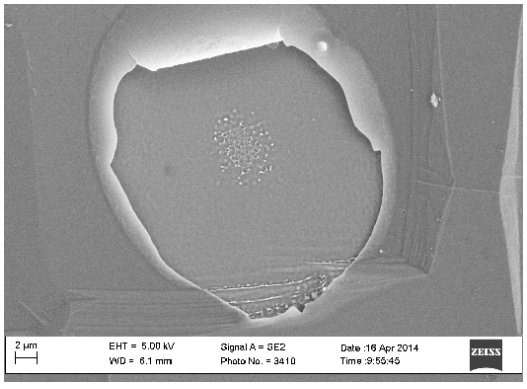

Figure 5.8: Damage to the silicon substrate.

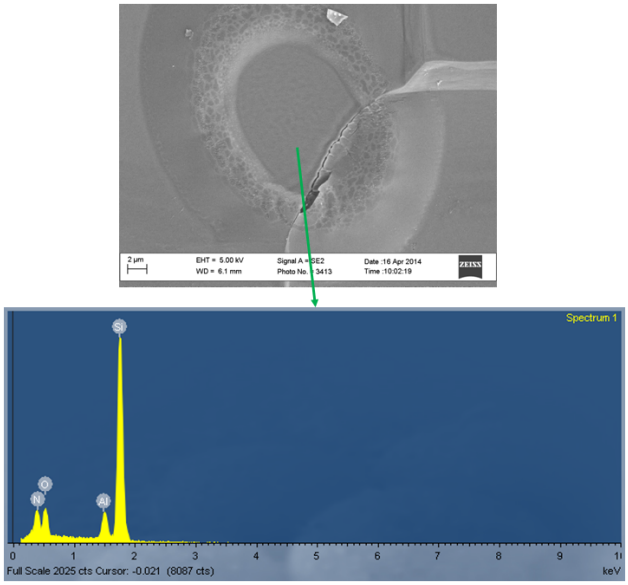

Figure 5.9: Elemental analysis of the central island.

Chapter 6

Interaction dependence on different parameters.

6.1 Pulse duration.

By changing the pulse time width, the parameters that describe the interaction between the material and the light change. In fact, the probability of the absorption phenomena changes, and therefore, also which phenomena are dominant and which negligible. Up to temporal widths of a few tens of picoseconds the pulse is located in the ultrafast regime but, as the time length increases, it approaches the regime of long pulses. We expect, therefore, to find results similar to the previous even for samples processed with pulses of a few picoseconds.
In particular, it is of interest to know how the threshold fluence changes as a function of pulse duration. As a matter of fact, while in the regime of long pulses, by reducing the pulse duration the volume in which energy is deposed decreases, in the short pulse regime this volume is, in first approximation, determined only by the optical properties of the material.
For ultrafast laser interactions, therefore, the dependence of the damage threshold of the pulse duration deviates from the trend $\sqrt{\tau}$ valid in the long pulses regime, and this happens when the pulse duration is longer than the characteristic time for thermal diffusion.

To process the samples in the picosecond regime we used the parameters listed in table 6.1.

The samples were processed with four different duration of the pulses: 1 ps, 2 ps, 4 ps, 6 ps. For all the processed samples we have found results in agreement with the analysis made in the femtosecond regime and, therefore, with the 'lift-off' process. In figure 6.1 and 6.2 examples are given of delam-

Wavelength	1028 nm
Average power	$0 - 1$ W
Frequency of the pulses	10 kHz
Maximum energy for pulse	0.1 mJ
Focal lens	500 mm

Table 6.1: Used values in the picosecond regime.

inated laser spot in all four time regimes. Delamination occurs cleanly and very well defined.

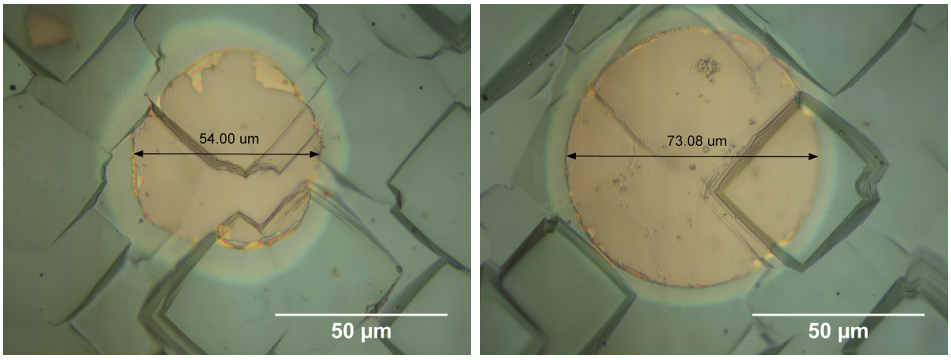

Figure 6.1: Spot corresponding to a temporal width of 1ps and power 370mW (left) and spot of 2ps with 520mW (right).

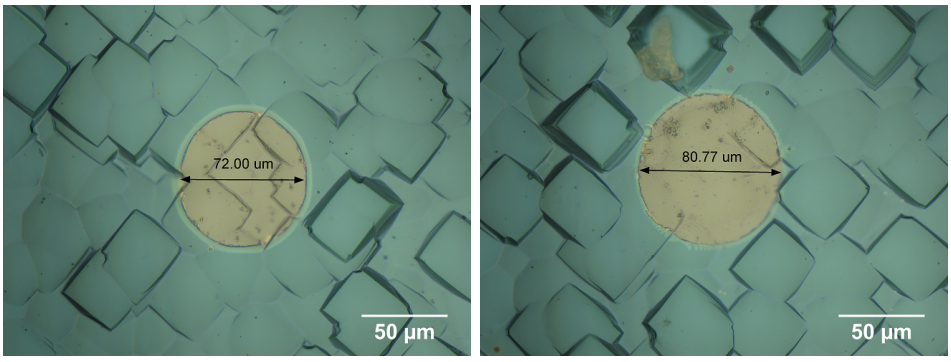

Figure 6.2: Spot corresponding to a temporal width of 4ps and power 580mW (left) and spot of 6ps with 700mW (right).

In analogy to what was done in the femtosecond regime, even in this

case, we proceeded with the analysis of the threshold delamination fluence $\Phi_{\text{th,b}}$ (section 5.1). The results obtained are shown in figure 6.3 and in the table 6.2.

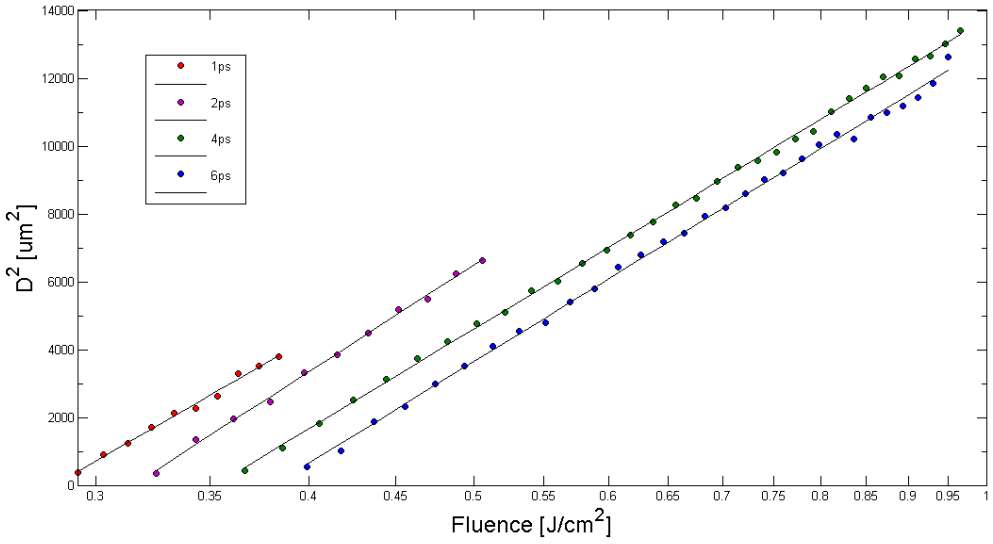

Figure 6.3: Square of the diameters of delaminated spots as a function of fluence for different time width. The fluence scale is logaritmic.

τ	$\Phi_{\text{th,b}}$ [mJ/cm^2]
1ps	283.64±47.13
2ps	315.50±41.84
4ps	352.76±15.46
6ps	381.18±27.15

Table 6.2: Value of the threshold fluences for the delamination at different temporal width for the pulses.

While the length of the pulse increase, the plasma density in the material progressively decrease. This causes the lower ability of the plasma to attenuate the pulse by locating at the interface the energy deposition process of the beam. This translates into an ablation threshold that increase with pulse length as shown in figure 6.4.

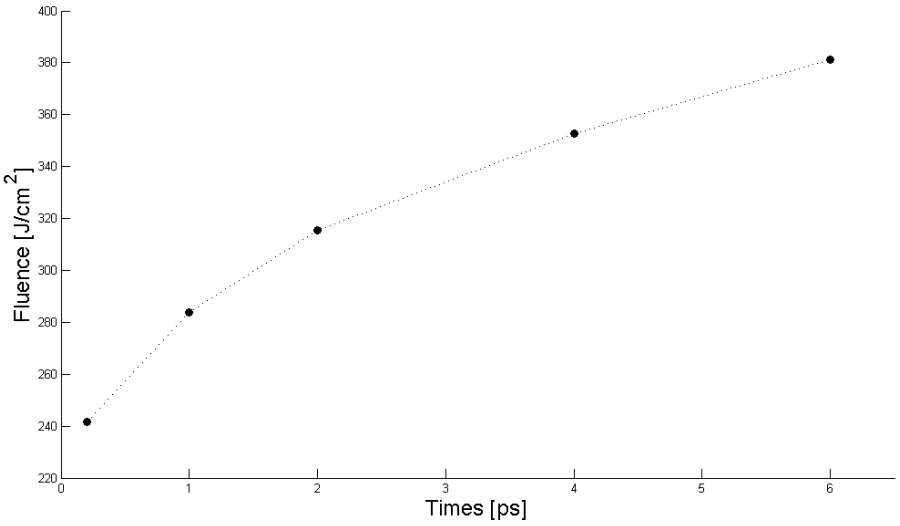

Figure 6.4: Threshold fluence as a function of pulse duration.

6.2 Free carriers lifetime.

The passivation layers located on the back side of the cell have the function of reducing recombination effects due to the limited dimension of the object and consequentially to the presence of a surface. By reducing the recombination the lifetime of the carriers increase and this allows a better recovery of the signal.
To be able to verify that the indirect ablation process is a good candidate for a method to process high efficiency cells, the first objective is to control that there is an efficient removal of the dielectric material. As a consequence, there is a reduction in the lifetime of the carriers. Therefore, if the removal of the passivation material, already demonstrated dy the EDX analisys, goes cleanly it will leads to have a portion of uncovered silicon, where subsequentially the contacts will be deposed. In this areas, the carriers tend to recombine more thanks to the discontinuity due to the surface and so their average lifetime will decrease.
Samples of 4x4 cm have been analyzed, on these an area around the 3% of the total was uncovered. In the table 6.3 is reported the average lifetime of the carriers before opening the contacts τ_1 and after τ_2:

pulse duration	$\tau_1[\mu s]$	$\tau_2[\mu s]$
200fs	35.06	23.26
1ps	36.92	25.46
4ps	30.98	20.68
10ps	45.70	27.46

Table 6.3: Lifetime of the carriers before opening the contacts and after.

From the data is clear that there is a decrease in the effect of the passivation: the lifetime of the carriers is decreased of about 30%. This reduction do not seem to depend on the length of the pulses, but only from the value of the delaminated area as it was expected.

For the reported analysis it was used a photoluminescence detector (WCT-120PL, Sinton Instruments).

6.3 Wavelength.

A very important parameter of the used laser source is the wavelength. To obtain the lift-off process is absolutely necessary that most of the energy is absorbed by the silicon substrate and not by the dielectric layers. As seen in figure 3.5, if the light interacts with the dielectric layers the delamination may be partial or absent.
The passivation on the back of the photovoltaic PERC cells that we used, is made of a SiN_x layer (refractive index about 2.05) and of one of Al_2O_3 (refractive index about 1.70). These materials are both opaque to visible light. The layers that make up the passivation are of the order of tens nanometers, and, therefore, the absorption within them will be strongly dependent on their thickness [35]. Despite this, we expected that by using wavelengths in the visible there would be a significant probability of having the same absorption in the dielectric and that only a part of the energy deposited would arrive to the underlying silicon [36].

In figure 6.5 are shown the images of the samples processed at different fluences having changed the wavelength of the laser source from1028 nm to 515 nm (green light).

Part of the pulse energy is deposed in the dielectric, so that direct ablation in the center of the spot occurs. Direct ablation follows the energy distribution, in this way a clean removal is impossible. It is not possible to obtain indirect delamination on the entire spot area with a gaussian energy distribution, because the delamination threshold is too close to the threshold

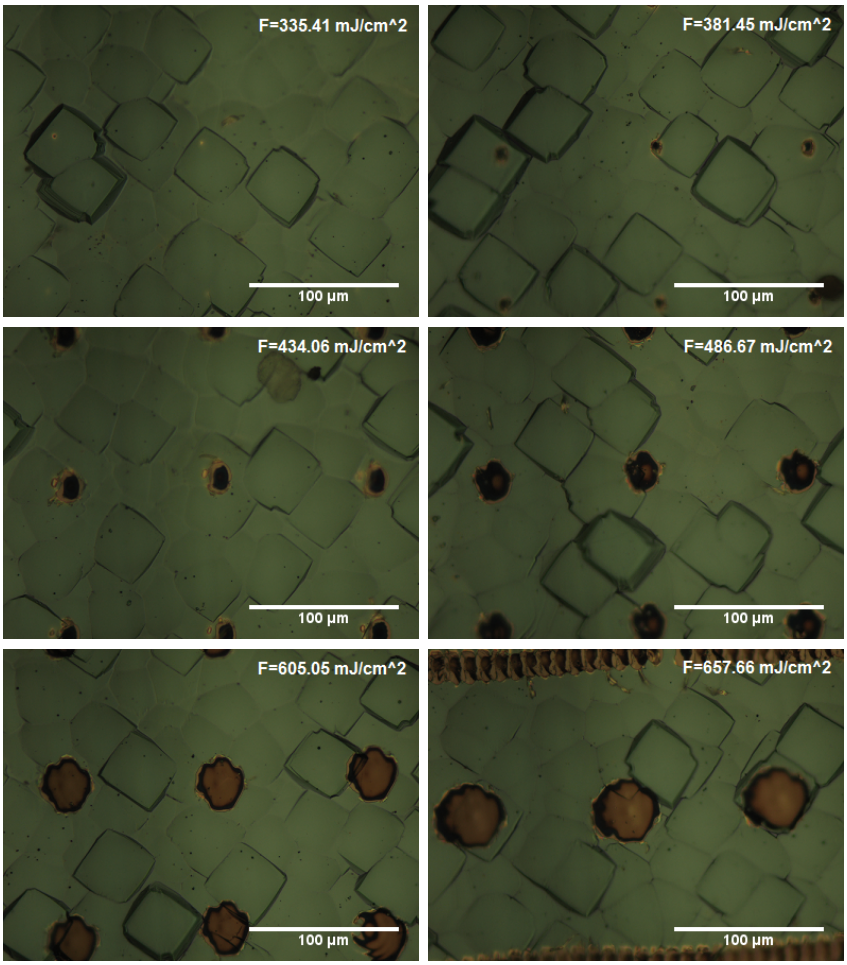

Figure 6.5: Dynamics of the interaction at increasing fluences F for $\lambda = 515\,\text{nm}$.

for dielectric damage, since the photon energy is greater than in the fundamental wavelength case. This is all in accordance with the model of the lift-off.

6.4 Texturing

Another element that results to be fundamental in the studied delamination phenomenon is the surface of the material. We know that in the front side of the solar cell the silicon is chemically etched to increase the internal reflections of light. We talk about texture in this case. The back side of the

cell can be textured or not.
Therefore we have studied the dependence of the interaction with this kind of surface. The figures 6.6 and 6.8 show the profilometer analysis of a 250x250μm area for both cells.

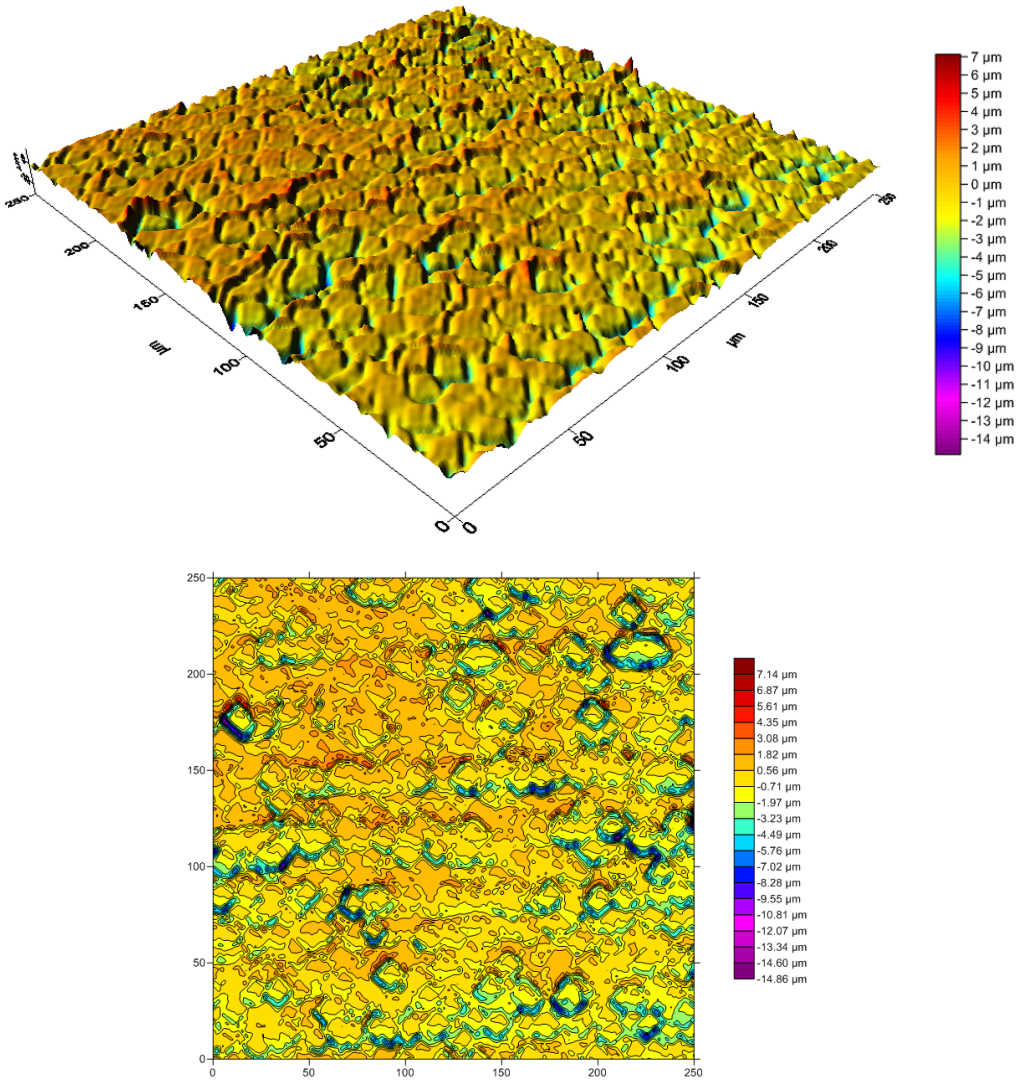

Figure 6.6: Surface of non-texturized cell, minimum step of the profilometer 1 μm.

The cell without texture presents a surface with an average roughness of $R_a = 1.16$ and a root mean squared roughness of $R_q = 1.60$, where these quantities where calculated as:

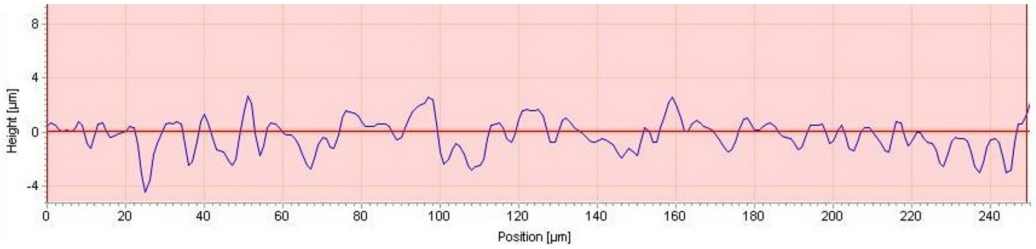

Figure 6.7: Unidimensional profile of a lateral section of a non-texturized cell. The data are normalized in respect to the maximum height.

$$R_a = \frac{1}{n}\sum_{i=1}^{n}|y_i| \tag{6.1}$$

$$R_q = \sqrt{\frac{1}{n}\sum_{i=1}^{n}y_i^2} \tag{6.2}$$

where the y_i are the heights of the scanned points and n their number. The surface shows defects due to the fact that the silicon was not smoothed, but no texture is present. The average distance between peaks and valleys does no get above the $10\,\mu$m and the profile reported in figure 6.7 is fairly blunt.

Contrarily, the surface with texture has a much higher average roughness of $R_a = 2.31$ and root mean squared roughness $R_q = 3.01$. The reported lateral section in figure 6.9 show a more irregular trend than the previous surface. There are a sequence of peaks and valleys with a much higher slope. The average distance between peaks and valleys reach the value of $20\,\mu$m.

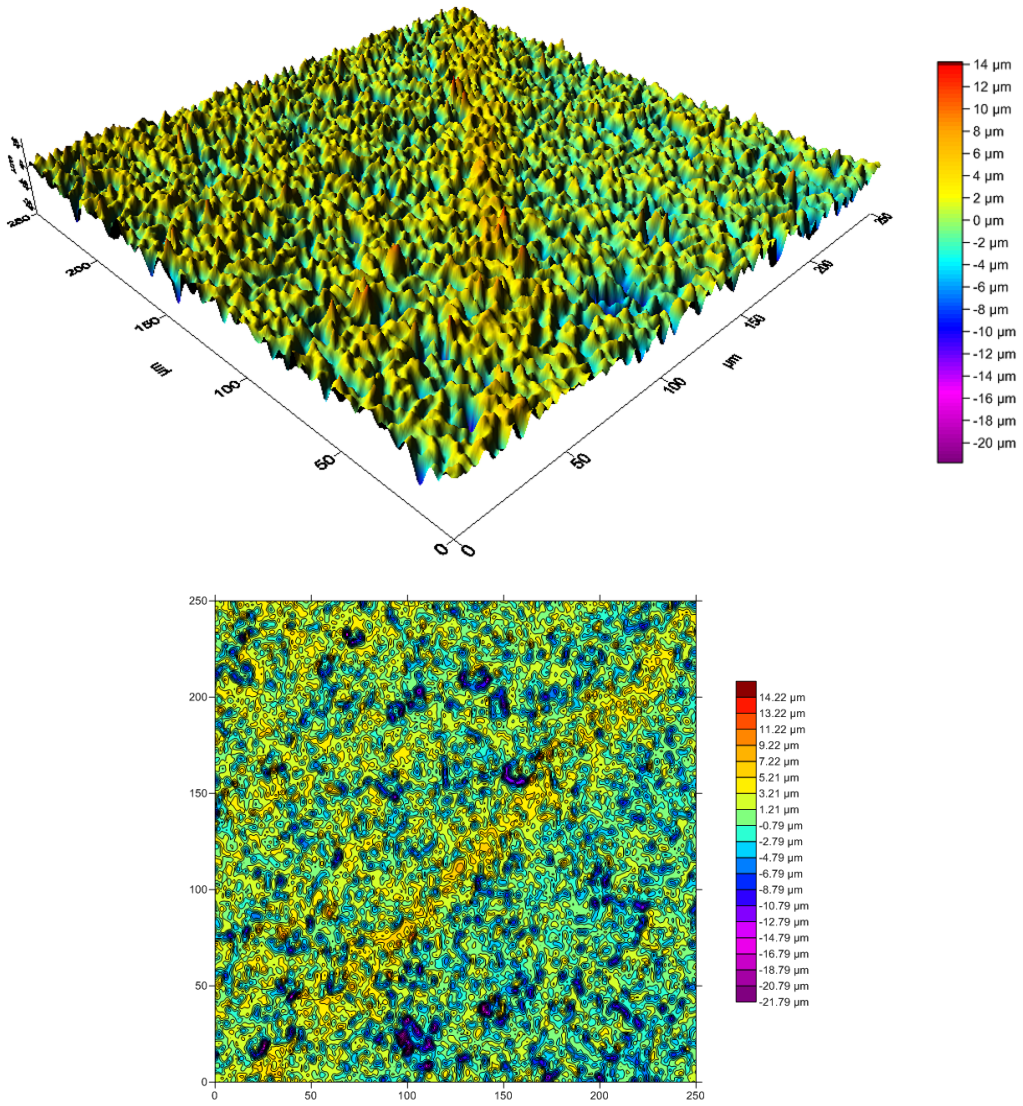

Figure 6.8: Cell surface with texture, minimum step of the profilometer 1 μm..

Notably, in the case of a perfectly flat surface, the area interested by the laser light is equal to the beam area, in perfectly perpendicular conditions. But when there is an irregular surface the area that is interested by the beam will be greater than its dimensions. To address this problem we can define the parameter γ as the inverse of the ratio between the area of the interested surface and the area of the beam:

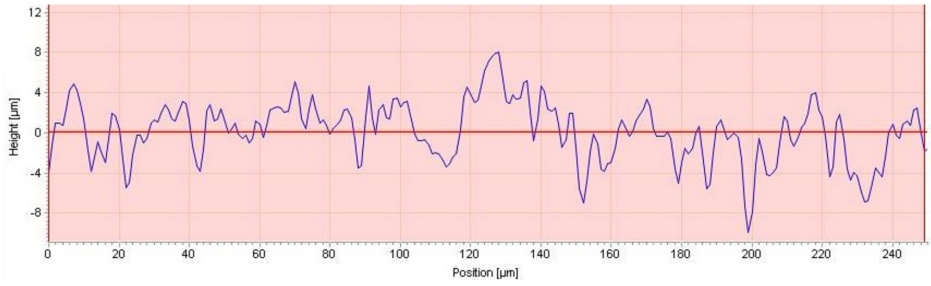

Figure 6.9: Profile of a section of the texturized cell. The data are normalized in respect to the most high peak of the surface.

$$\frac{1}{\gamma} = \frac{\pi r^2}{\pi \rho^2} \tag{6.3}$$

where r is the radius of the spot on the material and ρ the beam radius on the perpendicular plane in respect to the propagation direction. If the ratio γ is equal to one the surface would be ideally flat, instead if γ increase the surface will have a higher roughness.
To experimentally calculate this parameter different acquisition from the profilometer of different zone of the same cell have been made, in this way it is possible to have a general trend of the whole surface. The values that results from the analisys of 10 different acquisitions, each one of a 1x1 mm surface, for every kind of cell are:

$$\begin{aligned} \gamma_{\text{notexture}} &= 2.50 \pm 0.05 \\ \gamma_{\text{texture}} &= 1.47 \pm 0.03 \end{aligned}$$

Fluence analysis with rough surfaces. The analisys of the threshold fluence done in the chapter 5.1 does not consider the kind of surface on which the interaction happens. In the case of a non-ideally flat surface the equation 5.1 that calculates the beam fluence as a function of the spot radius on the material can be expressed in this approximation as:

$$\begin{aligned} \phi(r) &= \phi(0) \exp\left(-2 \cdot \frac{r^2}{w_0^2}\right) \\ &= \phi(0) \exp\left(-2 \cdot \frac{\rho^2}{\gamma w_0^2}\right) \end{aligned} \tag{6.4}$$

With this new definition, it is easy to show that the equation 5.4 becomes:

$$\begin{aligned} D_{\text{th}}^2 &= 2w_0^2\left[\gamma \ln \phi_0\right] - 2w_0^2\left[\gamma \ln \phi_{\text{th}}\right] \\ &= 2w_0^2 \ln\left(\phi_0^{\gamma}\right) - 2w_0^2 \ln\left(\phi_{\text{th}}^{\gamma}\right) \end{aligned} \tag{6.5}$$

Therefore the fluence have to be corrected with the γ parameter that best describe the kind of surface with which there is interaction.

For example, considering the case of ultrafast pulses of temporal length 200 fs on a cell without texture: the delamination threshold with the material corresponds to $\phi_{\text{th,b}}^{*} = (241.50 \pm 47.13)\,\text{mJ/cm}^2$, in other words around $3\,\mu$J of pulse energy. This value can be rewritten as:

$$\phi_{\text{th,m}}^{*} = \left(\phi_{\text{th,m}}\right)^{\gamma_1} \tag{6.6}$$

where γ_1 is the parameter of the surface for solar cells without texture and $\phi_{\text{th,m}}$ is the real fluence of the laser source. If we used this fluence on a textured surface we will get:

$$\bar{\phi}_{\text{th,m}} = \left(\phi_{\text{th,m}}\right)^{\gamma_2} = \left(\phi_{\text{th,m}}^{*}\right)^{\gamma_2/\gamma_1} \tag{6.7}$$

where γ_2 is the surface parameter of texturized cells. By replacing the found values we get $\bar{\phi} = 25.19\,\text{mJ/cm}^2$. This fluence is much lower than the one before. This is obvious because if, with the same deposed energy, the interested area increase then the fluence must necessarily decrease. This imply that deposing $3\,\mu$J of pulse energy with a $w_0 = 36.80\,\mu$m on a cell without texture there is the delamination effect, but in a texturized cell you have to be much more aggressive.

Our reasoning does not consider the way in which the energy is distributed, because on a surface that is not smoothed the intensity profile of the typical Gaussian beam will depose on a sequence of peaks and valleys and therefore the intensity will not be uniform. The data we obtained is indicative of the fact that in conditions of texturized surfaces or others roughness elements other regimes are favoured instead of the lift-off one.

From the sample analisys on cells of this kind we get results that are in agreement with the previous statement: at fluence of the order of hundreds of mJ/cm^2, typical of the lift-off phenomen, only a variation of the material refraction index is seen but not an effective damage of the surface, as shown in figure 6.10.

If you switch to higher fluences you get different regimes of interaction of which examples are shown in figure 6.11, 6.12 and 6.13 for different energy pulse, repetition rate and number of pulses.

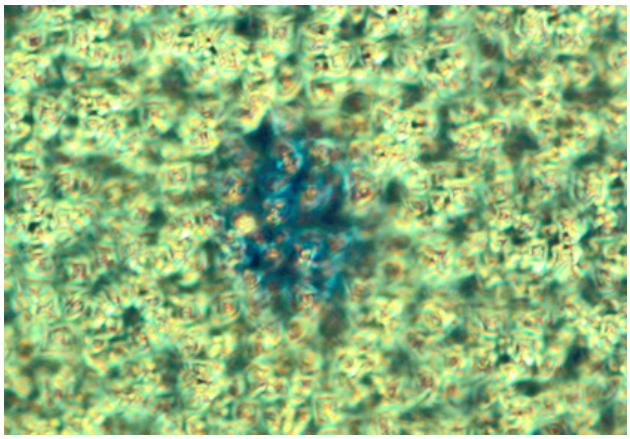

Figure 6.10: Optical microscope photo of a spot on a texturized cell at 200 fs with a fluence of 402 mJ/cm^2.

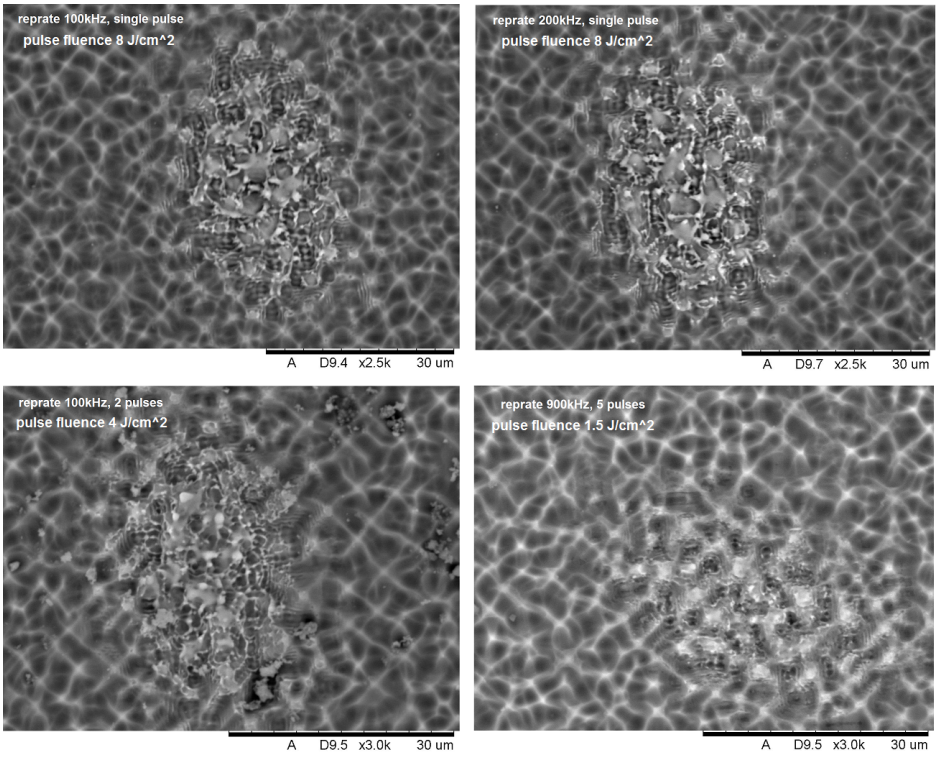

Figure 6.11: Electronic microscope images of samples processed with pulses of length 200 fs and $w_0 = 17.79\,\mu$m. Total energy deposed 0.04 mJ.

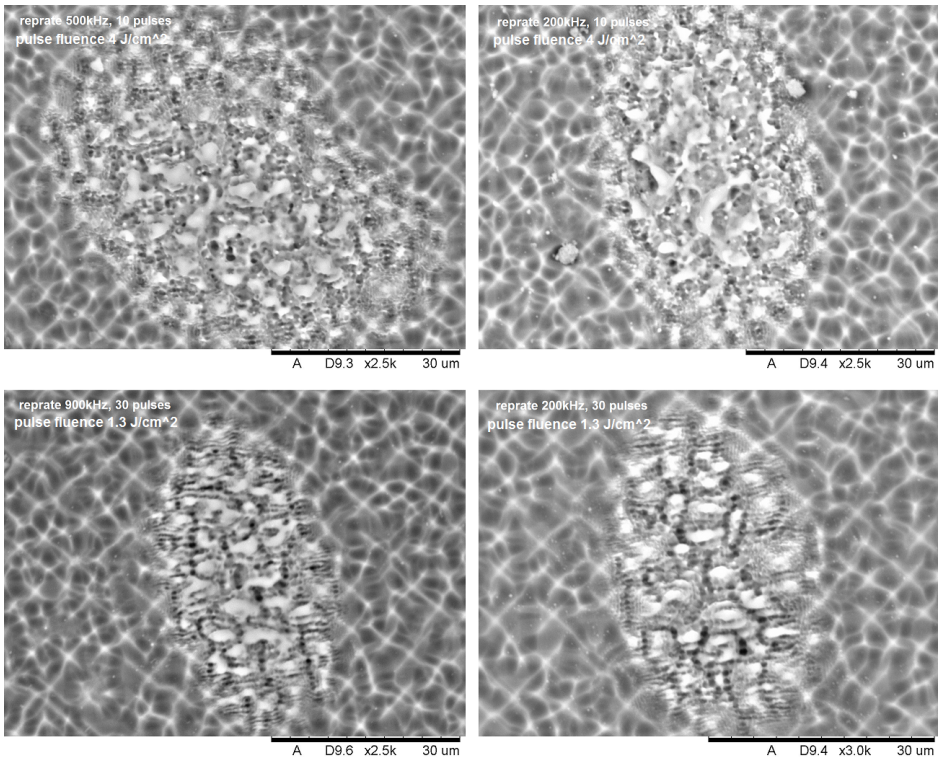

Figure 6.12: Electronic microscope images of samples processed with pulses of length 200 fs and $w_0 = 17.79\,\mu$m. Total energy deposed 0.2 mJ.

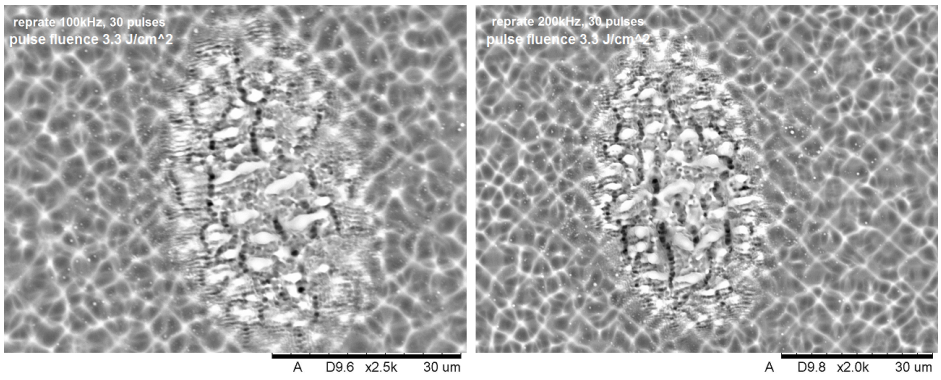

Figure 6.13: Electronic microscope images of samples processed with pulses of length 200 fs and $w_0 = 17.79\,\mu$m. Total energy deposed 0.5 mJ.

The interaction, in this case, is distinctly different from that in the case of non-texturized surfaces. With increasing energy deposed the damage to the material grows but the geometry does not allow to have clean and completely delaminated spots. The EDX analisys, of which an example is shown in figure 6.14, show the partial removal of dielectric material principally on the peaks of the surfaces. This removal can happen in principle thanks to the lift-off process, but since the used fluences are all above 1 mJ/cm^2 it is extremely probable that the interaction will lead to the direct ablation of the passivation material.

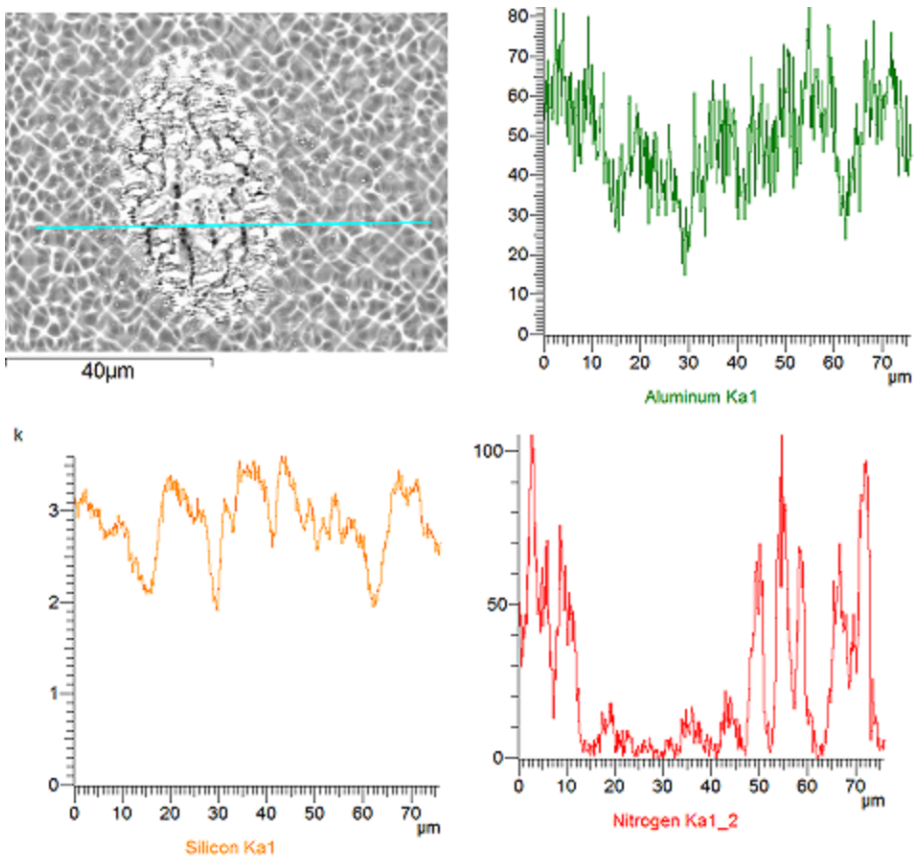

Figure 6.14: EDX analysis of a texturized cell sample processed with laser source parameters of 200 fs pulse length, 200 kHz repetition rate, 30 number of pulses, 3.3 J/cm^2 single pulse fluence.

Changing the energy of the single pulse is, obviously, more or less aggressive but also the repetition rate results to be fundamental. In figure 6.15 is reported an example of high repetition rate, 900 kHz, at comparison with

a sample processed with a low repetition rate, 100 kHz, for the same total energy deposed and comparable pulse energy.

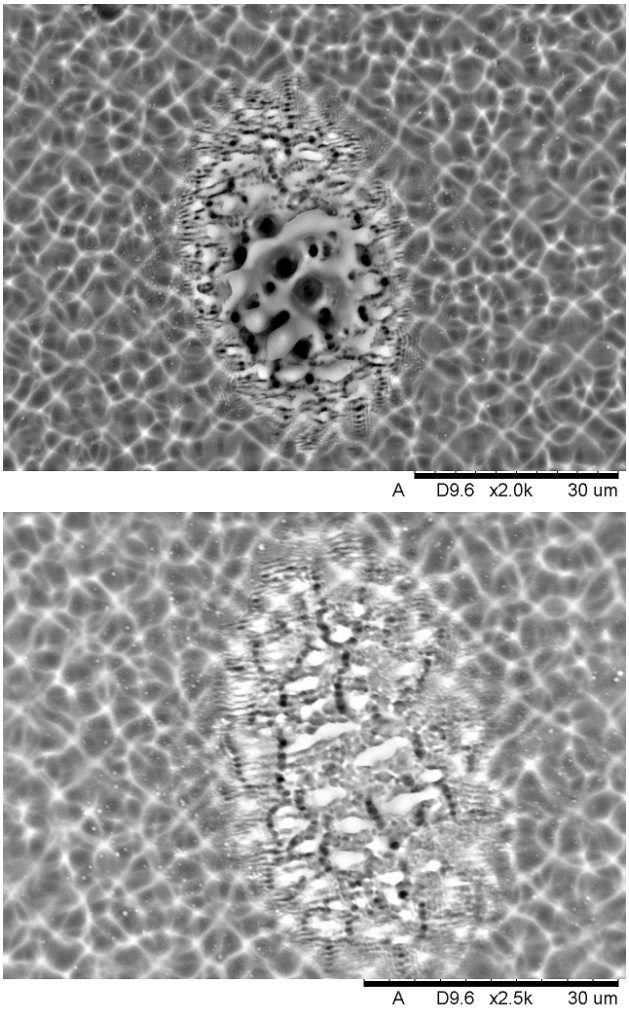

Figure 6.15: Top , SEM image of a sample processed with 50 pulses each one with a fluence of 2 J/cm^2, pulse length 200 fs, 900 kHz repetition rate. Bottom, sample with pulses at 3.2 J/cm^2 and number of pulses at 30. Pulse length 200 fs, 100 kHz repetition rate. Total energy deposed in both cases 0.5 mJ.

In the case of an higher repetition rate (top in figure 6.15) the material is damaged more and, probably, melted in the central zone of the spot. In the case of a lower repetition rate (bottom in figure 6.15), the same condition is not reached even if the pulses are more energetic. This could be due to the

fact that making the pulses temporally closer is going to favor the thermal effects that in the ultrafast interaction are usually not dominant. In this way seems to be more aggressive the situation where the energy is deposed in the shortest time possible.

Chapter 7

Electric properties.

In order to effectively introduce a method of machining with ultrafast laser in the production of PERC photovoltaic cells, it is necessary to study the characteristics of a processed cell by the electric point of view. The standards to ensure are definitely high precision work, a good contacting and the ability to sustain the pace dictated by the production line.

7.1 Contacts geometry.

A fundamental aspect to realize a complete device is the pattern into which the contacts are deposed. The optimal situation will be the one where there is a perfect equilibrium between the losses, due to the removal of the passivation, and the collection of the signal. To have good contacts it is essential to favor the formation of the Al-Si alloy that is the basis of BSF (section 2.2) limiting as much as possible the area in which the passivant is removed.
On the contacts geometry there are numerous studies ([37] [38] [19]), our choice was to process the cells with channels of width around 30 μm and 900 μm distant from each other, as shown in figure 7.1 and 7.2. The channels are made from many overlapped spots. The distance between two spots has been calculated as the 20% of the diameter. The fluence of the spots was calculated with the analysis of section 5.1 in order to obtain the desired value for the diameter.

Samples with the same characteristics were processed with different time length of the pulses from 200 fs to 10 ps, 500 kHz repetition rate, 1028 nm wavelength. The results were rather homogeneous reflecting always a good contact opening. Some examples are reported in figure 7.3 and 7.4.

For increasing temporal lengths the thermal effects of the light-matter interaction also increase. An effect of this phenomen is shown in figure 7.5

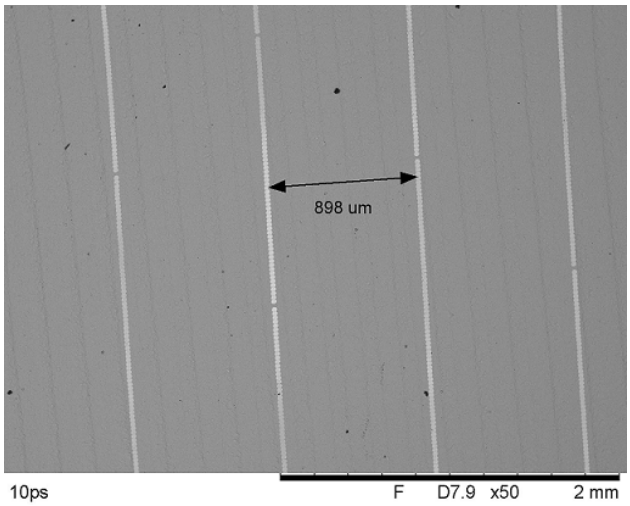

Figure 7.1: Distance between adjacent channels in a non-texturized sample processed with 10 ps pulses.

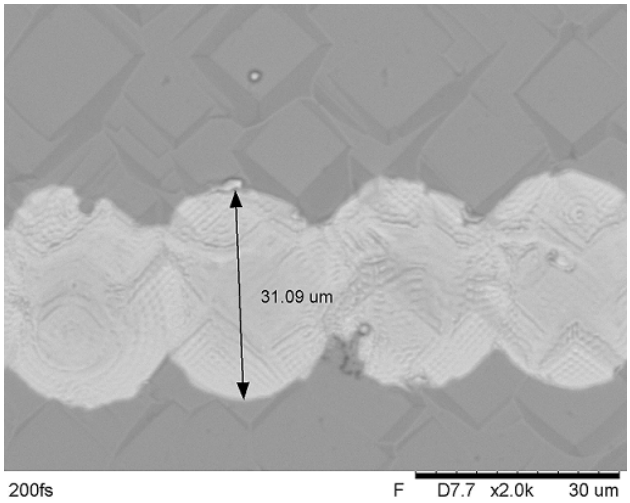

Figure 7.2: Maximum diameter of a channel in a non-texturized cell processed with 200 fs pulses.

where, in the particular case of 10 ps pulses, there was a damage to the material probably due to fusion phenomena.

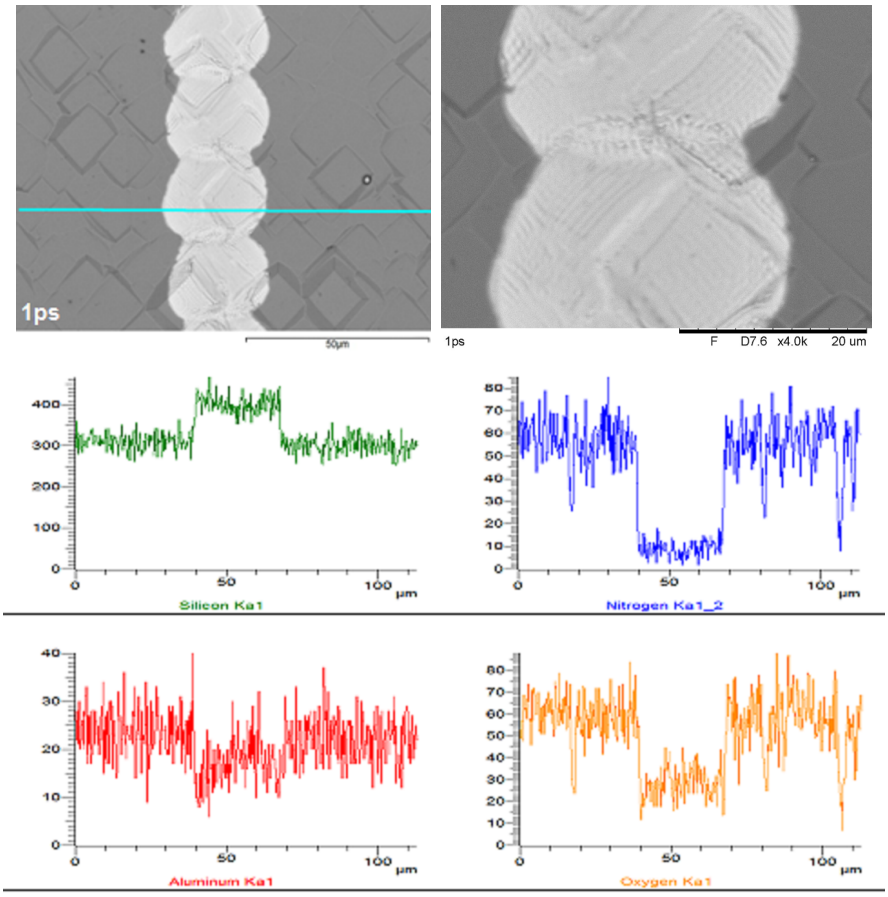

Figure 7.3: Channel in a non-texturized cell processed with 1 ps pulses, 4.9 W used power and 500 kHz repetition rate with EDX analysis of the blue line in figure.

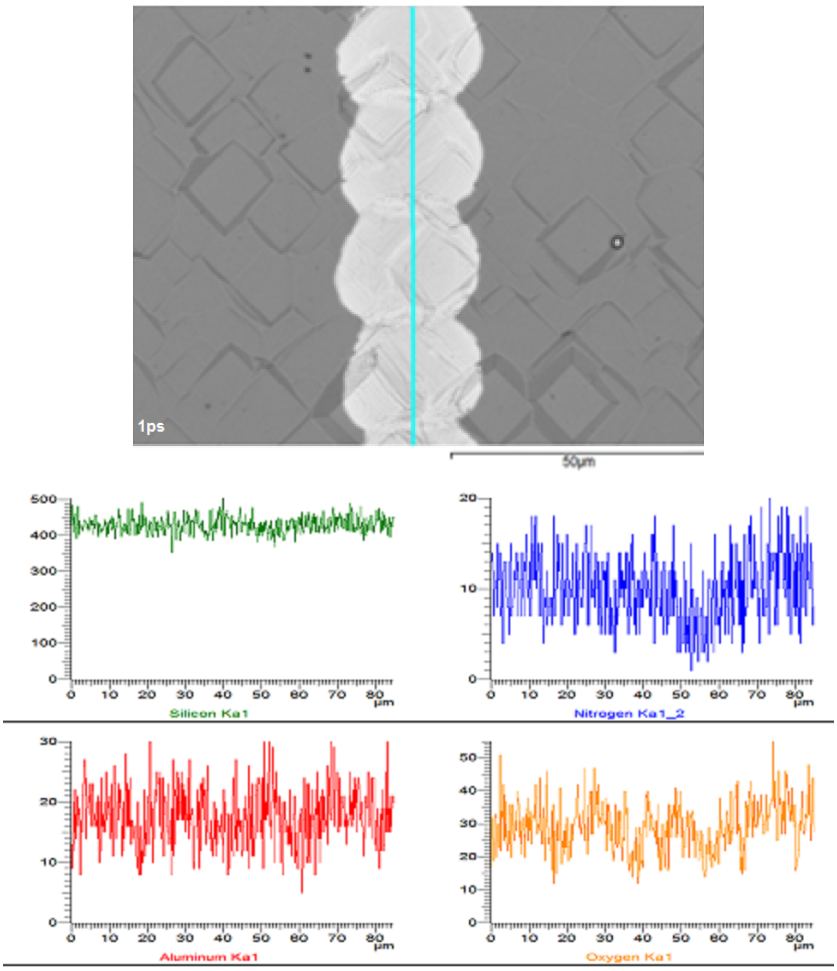

Figure 7.4: EDX analysis of a line inside the channel.

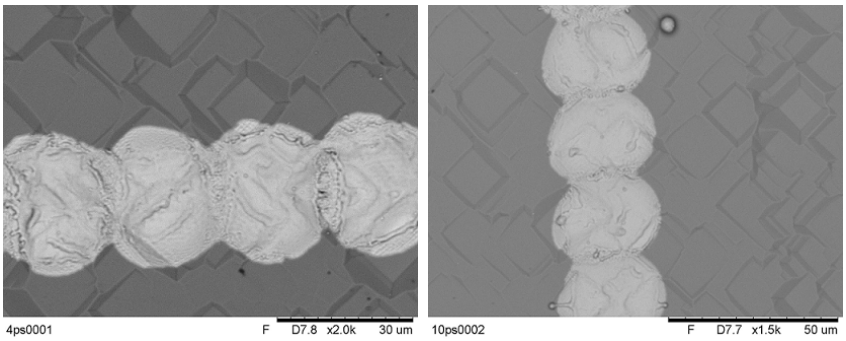

Figure 7.5: Channels on a non-texturized cell at 4 ps and 10 ps of time width.

Also in the case of cells with texture, the samples were processed with the same geometry. In this case it was preferred to change the repetition rate and number of pulses but leaving steady the pulse length at 200 fs and the wavelength at 1028 nm. An example is shown in figure 7.6.

An interesting comparison is that between the results obtained with the ultrafast source we used and a nanosecond source: $\lambda = 532$ wavelength, $\tau = 1$ ns pulse duration, $\nu = 600$ kHz repetition rate, 24 W max power. The analysis for the nanosecond source are reported in figure 7.7 and 7.8.
In the case of non-texturized cells the ultrafast source, thanks to the lift-off process, allows to obtain well delaminated spots, with clean borders and reducing at the minimum the thermal effects. Instead for the nanosecond source the thermal effects are more important. Even if it can ablate a good portion of the passivation layer the spots have less defined borders and the used energy is much higher than in the ultrafast case for the same spot dimensions. Compare, for example, the samples in figure 7.3 processed with a pulse energy around 0.01 mJ and that in figure 7.7 where the pulse energy is 4 times higher than in the ultrafast case.

Instead for the texturized cells the used fluence is the same both for the femtosecond and nanosecond source, figure 7.6 and 7.8. The removal of passivating material is never complete, but the samples processsed with longer pulses results to be more defined thanks to the thermal effects that damages more the material.

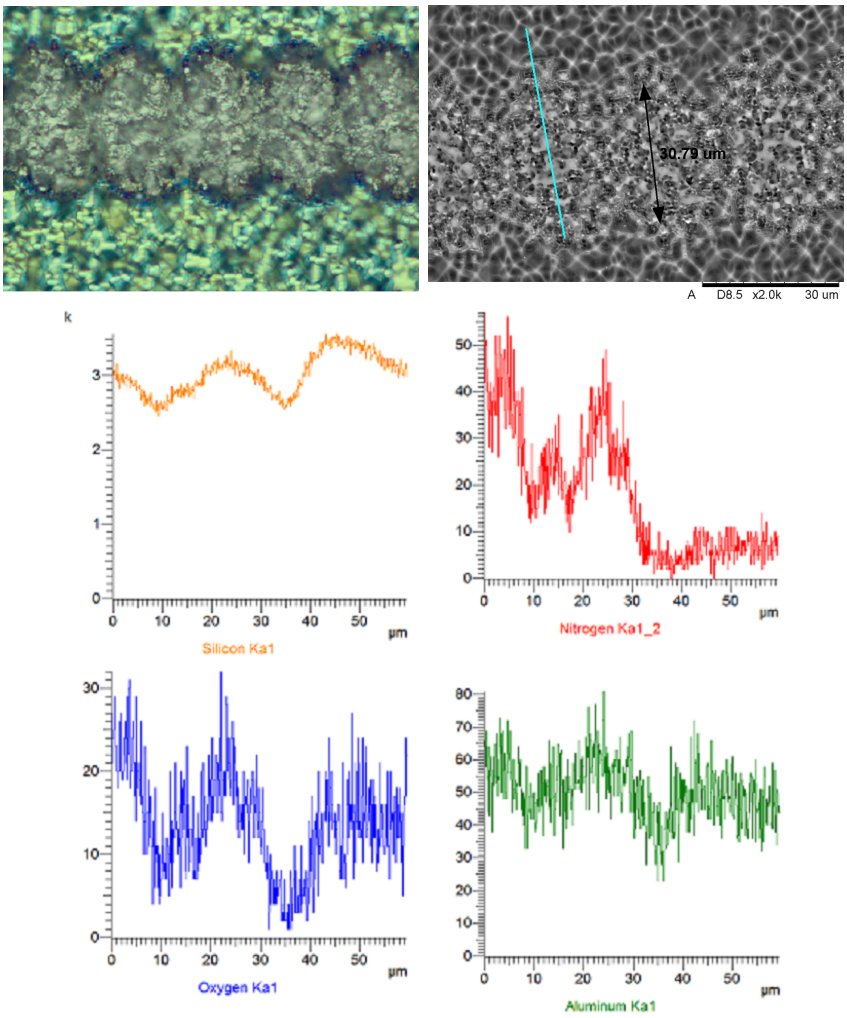

Figure 7.6: Texturized cell processed with a 500 kHz repetition rate and number of pulses equal to 5. Optical microscope image (left), electronic microscope (right) and EDX analysis (bottom).

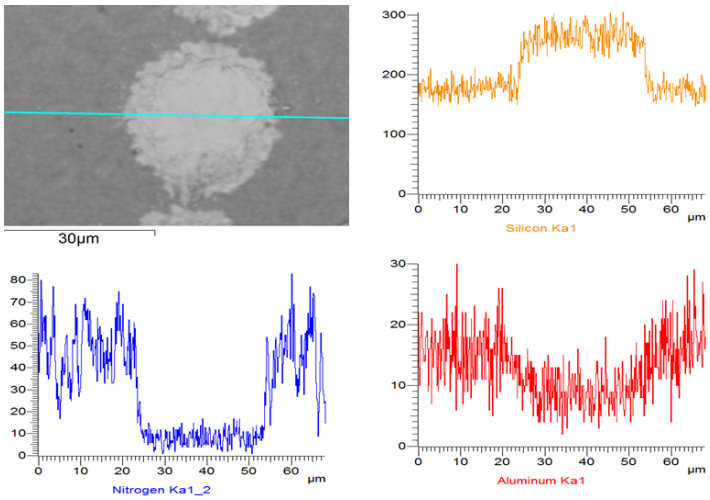

Figure 7.7: EDX analysis of test channels on cells without texture with the nanosecond source.

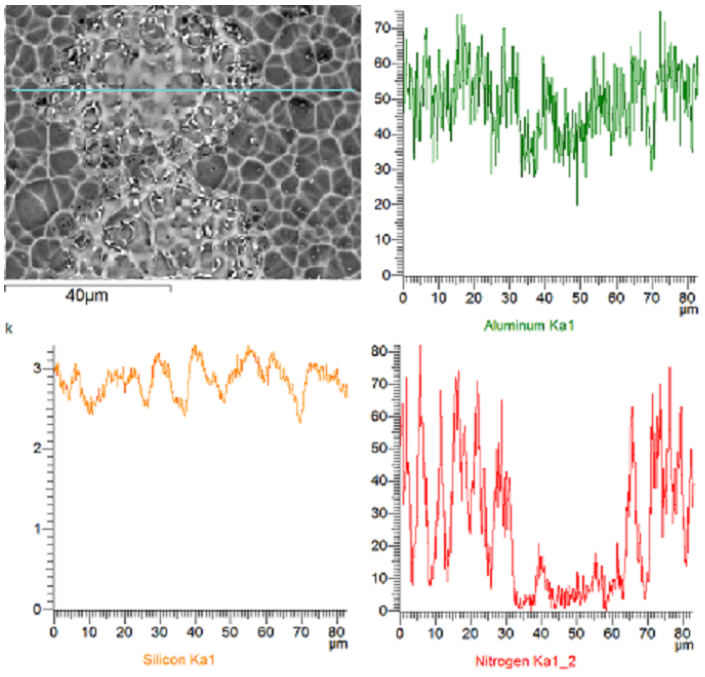

Figure 7.8: EDX analysis of test channels on cells with texture with the nanosecond source.

7.2 Efficiency of processed solar cells.

At this point of our study we switched to process complete cells and to characterize their electric properties. Unfortunately, it was possible to work only on devices with textured back for lack of other types of solar cells. The devices which have been characterized differ only for the laser source with which the contacts were opened on the back side of the cell. The used parameters are reported in Table 7.1.

	Pulse length	Wavelength	Reprate	# of pulses	Pulse energy
Batch 1	200 fs	1028 nm	200 kHz	2	20 μJ
Batch 2	200 fs	1028 nm	500 kHz	5	8 μJ
Batch 3	1 ns	535 nm	600 kHz	1	40 μJ

Table 7.1: Laser source parameter.

The work done is based on the comparison between the two types of laser source at the expense of the optimization on the production of solar cells and their metallization. A very important data is that the efficiency of the processed cells that, under no circumstances, exceeds the 19.2% when cells of this kind have an average efficiency over the 20%. Surely an optimization of the contacts printing could lead to higher efficiency values, as well as an optimization of the firing parameters. But the optimization of devices do not affect our study that wants to highlight the differences between the different ablation techniques.
Therefore we report some of the most significant parameters for the characterization of the solar cells functionality. The data, figure 7.9 7.10 7.11, are normalized in respect to the maximum value to have a better comparison.

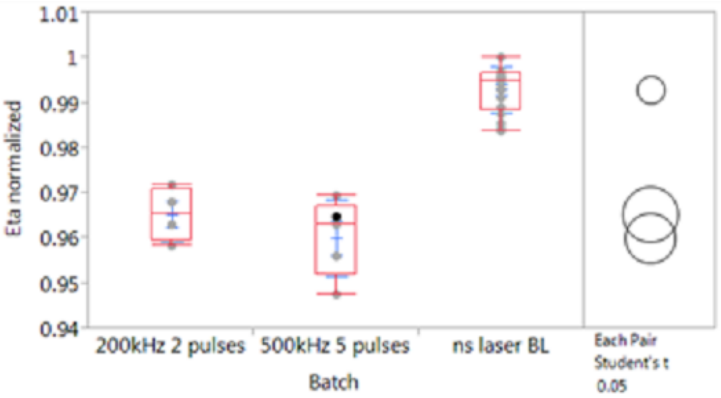

Means and Std Deviations

Level	Number	Mean	Std Dev	Std Err Mean	Lower 95%	Upper 95%
200kHz 2 pulses	4	0.965249	0.005855	0.00293	0.95593	0.97457
500kHz 5 pulses	5	0.960204	0.008507	0.00380	0.94964	0.97077
ns laser BL	17	0.992942	0.005184	0.00126	0.99028	0.99561

Figure 7.9: Box plot for the efficiency value of the solar cell normalized in respect to the maximum value for each batch. The Student test shows the statistically compatible values.

The data are reported with a box plot: the line inside the box represents the median of the distribution, the lines external to the box represents the first an third quartile.
From the reported data it is clear that the cells processed with an ultrafast source have lower performance of the cells processed with longer pulses. The data that seems to better describe the phenomenon is the open circuit voltage that, as shown in figure 7.10, in the case of ultrafast pulses is lower. This value, usually, denote the partial removal of the dielectric layer. The presence of the passivant leads to an increase of V_{oc}, but a poor removal of the passivation layer leads to a sharp fall of this value. This could explain the efficiency decrease of the cells processed with the ultrafast source compared to the other as also the EDX analysis (see figure 7.6) shows a non-total ablation of the dielectric material.
Results would be expected, therefore, to be much more favorable in the case of cells without texture where the ultrafast source manages to reach the complete removal of the passivating material.

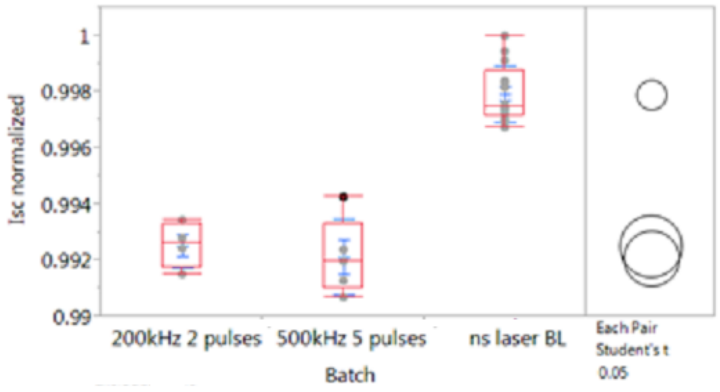

Means and Std Deviations

Level	Number	Mean	Std Dev	Std Err Mean	Lower 95%	Upper 95%
200kHz 2 pulses	4	0.992543	0.000816	0.00041	0.99124	0.99384
500kHz 5 pulses	5	0.992120	0.001361	0.00061	0.99043	0.99381
ns laser BL	17	0.997940	0.001014	0.00025	0.99743	0.99846

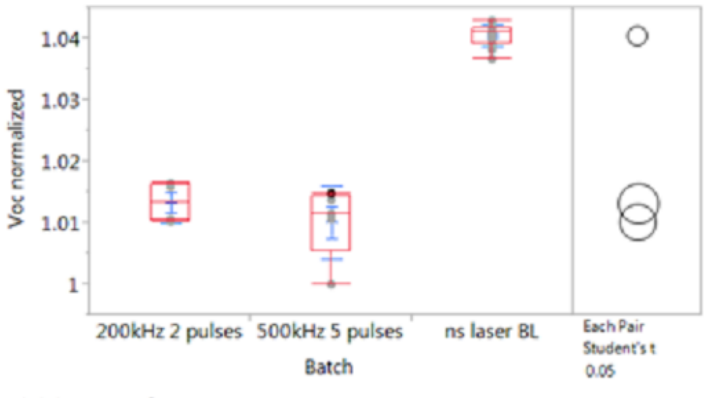

Means and Std Deviations

Level	Number	Mean	Std Dev	Std Err Mean	Lower 95%	Upper 95%
200kHz 2 pulses	4	1.01335	0.003300	0.00165	1.0081	1.0186
500kHz 5 pulses	5	1.01016	0.005927	0.00265	1.0028	1.0175
ns laser BL	17	1.04050	0.001730	0.00042	1.0396	1.0414

Figure 7.10: Value of the short-circuit current I_{sc} and open circuit voltage V_{oc}.

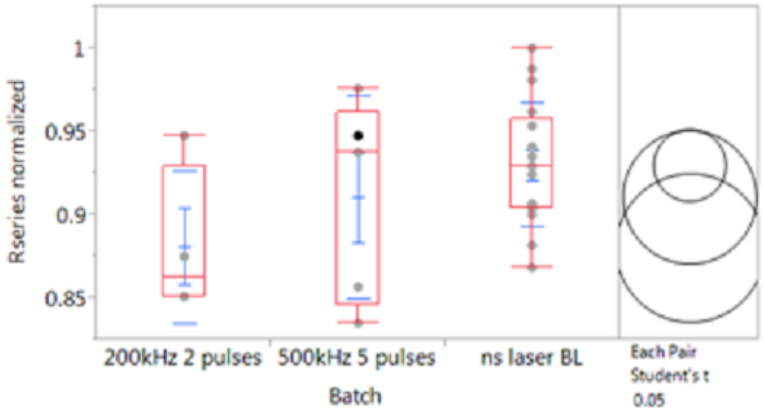

Means and Std Deviations

Level	Number	Mean	Std Dev	Std Err Mean	Lower 95%	Upper 95%
200kHz 2 pulses	4	0.880998	0.045786	0.02289	0.80814	0.95385
500kHz 5 pulses	5	0.910548	0.060889	0.02723	0.83494	0.98615
ns laser BL	17	0.930170	0.037070	0.00899	0.91111	0.94923

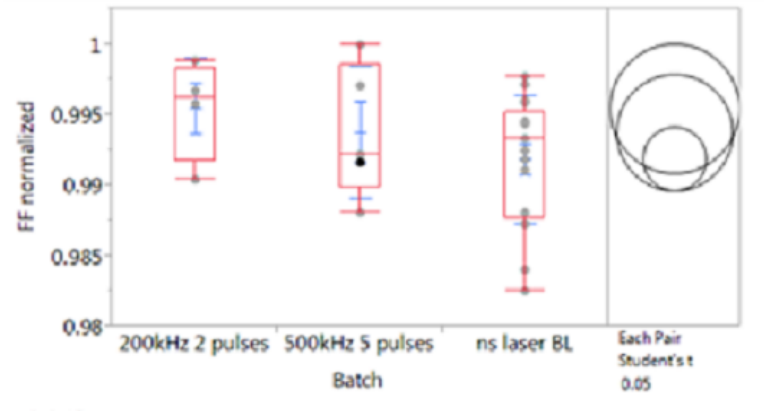

Means and Std Deviations

Level	Number	Mean	Std Dev	Std Err Mean	Lower 95%	Upper 95%
200kHz 2 pulses	4	0.995436	0.003585	0.00179	0.98973	1.0011
500kHz 5 pulses	5	0.993779	0.004727	0.00211	0.98791	0.9996
ns laser BL	17	0.991879	0.004534	0.00110	0.98955	0.9942

Figure 7.11: Fill factor and series resistance.

7.3 Parameter for the production line.

For the industrial production of photovoltaics cells are needed working standards that, obviously, are not required in the study performed in laboratory. In particular, the most strict requirement is the time needed for the work. A production chain in full capacity has a yield of one cell per second.
To satisfy this requirement it was assumed that also the opening of the contacts have to be completed in one second, in this way it would be a single step in the processing. We fix the time for the work at $t = 1s$ and the percentage of area that want to be uncovered for the contacts, for example, the 4% ot the total area. As seen in section 7.1, the geometry of the contacts has been fixed to channel of minimum width $d_{\text{min}} = 30\,\mu\text{m}$. On the basis of these parameters we have been looking for the characteristics of the experimental apparatus that would allow to process the cells in the way and whithin the timeframe required.

7.3.1 Gaussian VS flat top profile.

In the case of having to work with a Gaussian beam it is known that just the energy above the interaction threshold $\phi_{\text{th,b}}$ will contribute to the delamination.

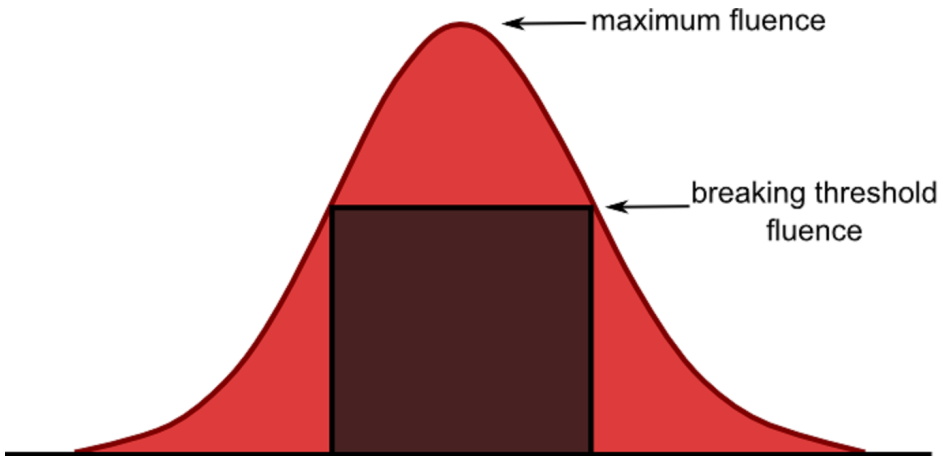

Figure 7.12: Difference between a gaussian profile (red) and a flat-top one (black).

Assuming you want to have channels of a diameter D on the material, from the equation 5.2 you get that the peak energy to use for a Gaussian beam E_{gaussian} have to be:

$$\begin{aligned} E_{\text{gaussian}} &= \frac{1}{2}\pi w_0^2 \phi_0 \\ \phi_0 &= \phi_{\text{th,b}} \exp\left(\frac{D^2}{2w_0^2}\right) \\ &< \phi_{\text{th,i}} \end{aligned} \tag{7.1}$$

where w_0 is the beam waist, ϕ_0 the peak fluence and $\phi_{\text{th,b}}$ the delamination threshold. Note that the peak fluence can not exceed the damage fluence $\phi_{\text{th,i}}$ to avoid the formation of the dielectric island.
On the contrary, if it was used a flat-top beam, the peak fluence would be equal to the breaking threshold and all the energy would be used for the delamination. In this case, to delaminate a spot of diameter D it would be sufficient the energy $E_{\text{flat-top}}$:

$$E_{\text{flat-top}} = \pi \phi_{\text{th,b}} \left(\frac{D}{2}\right)^2 \tag{7.2}$$

The condition in which you use the flat-top beam is energetically more convenient than that with a Gaussian beam. This concept is easy to express by calculating the ratio between the two calculated energies that, in the case where the damage fluence is not excedeed, do not depends anymore on the fluence threshold but only on the dimension of the beam and of the spots in the material. By defining x as the ratio between D and w_0, we get:

$$\frac{E_{\text{gaussian}}}{E_{\text{flat-top}}} = \frac{1}{2}x^2 \exp\left(-\frac{1}{2}x^2\right) \tag{7.3}$$

As it is clear from the figure 7.13 the function reported in equation 7.3 has a single maximum for $\bar{x} = 1.41$. This means that when $D = 1.41 \cdot w_0$ has been maximized the efficiency of the Gaussian beam in respect to the flat-top. Note that this maximum value corresponds to just the 35% of the efficiency of a perfectly flat-top beam, therefore a flat-top beam is surely to be preferred in respect to a Gaussian in threshold phenomena.

7.3.2 Gaussian beam.

In the case of non-texturized cells with a double layer of passivation, for a pulse length of 6 ps, it has been obtained that $\phi_{\text{th,b}} = 381\,\text{mJ/cm}^2$ and $\phi_{\text{th,i}} = 699\,\text{mJ/cm}^2$. These values give back a $\bar{x} = 1.11$ that fix the relation between D and w_0. Rember that neither D or w_0 are fixed, but only the relation between them. What is fixed is the minimum diameter of the channels d_{min}.

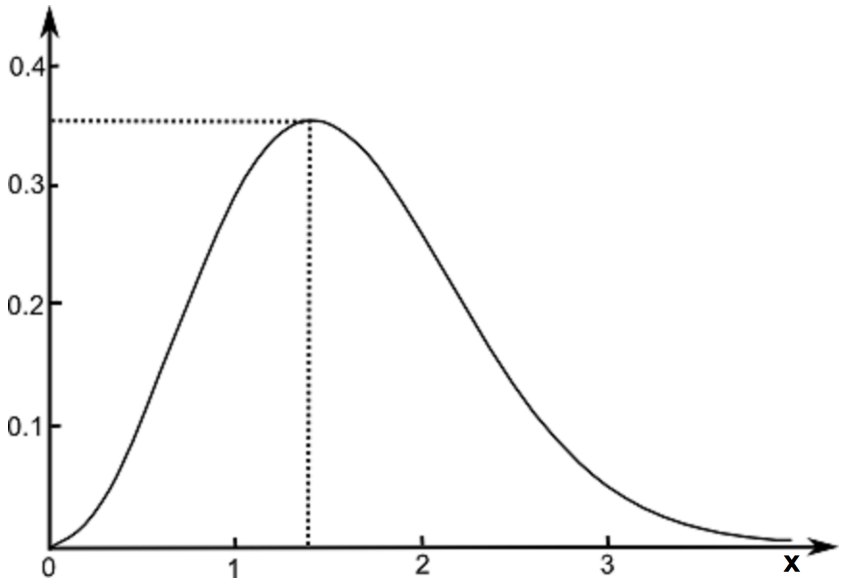

Figure 7.13: Graph of the function 7.3 which represents the efficiency of the Gaussian beam in respect to the flat-top one.

On these basis, it is possible to calculate the spacing between spots that allows to have the desired channels by variating the dimension D of the spots:

$$\text{spacing} = \sqrt{D^2 - d_{\text{min}}^2} \tag{7.4}$$

Similarly, it is possible to calculate the overlap that the spots must have between them. As shown in figure 7.14, the overlap between two spot is equal to twice the difference between the area of the circular sector highlighted in red and the area of the triangle in green. The area of the circular sector depends on the angle θ that can be calculated as $\theta = 2 \cdot \arctan(d_{\text{min}}/\text{spacing})$. From which:

$$\text{overlap} = 2 \cdot \left(\frac{\theta (D/2)^2}{2} - \frac{d_{\text{min}} \cdot \text{spacing}}{4} \right) \tag{7.5}$$

The area opened by a spot will be :

$$\text{OpenArea} = \pi \cdot \left(\frac{D}{2} \right)^2 - \text{overlap} \tag{7.6}$$

and the number of the spot n will be given by the total area that you want to open divided OpenArea. Knowing the number of spots it is possible

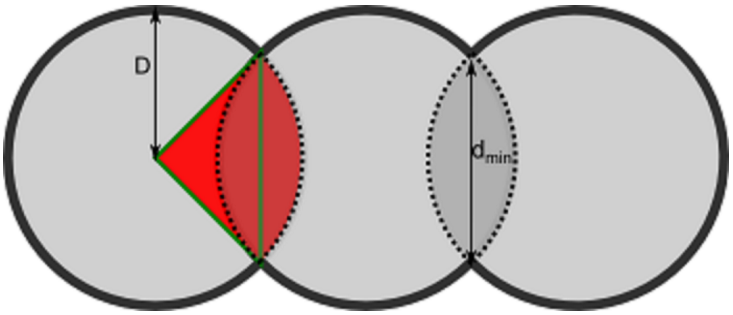

Figure 7.14: Overlap between two spot (dashed) as a difference between the area of the circular sector (red) and of the triangle (green).

to calculate the speed needed to move the beam v, the repetition rate ν and the power P of the source:

$$v = \text{spacing} \cdot \nu \tag{7.7}$$
$$\nu = \frac{n}{t} \tag{7.8}$$
$$P = E_{\text{gaussian}} \cdot \nu \tag{7.9}$$

Following are reported the values calculated of these quantities by varying the waist of the beam w_0, figure 7.16.

Note that the translation speed of the beam does not depend on the minimum dimension of the channels, since by increasing d_{min} the spacing decrease but the number of the spot increase and vice versa.

A possible choice for the production chain could be $w_0 \geq 0.01\,\text{cm}$ that corresponds to a translation speed under the 10 m/s achievable with galvonometric systems, a pulse energy of 0.1 mJ and 100 kHz of repetition rate.

7.3.3 Flat-top beam.

In the case of a perfectly flat-top beam, the diameter of the spot and the beam dimensions are the same and so the energy of the pulse will be given by the equation 7.2. The formulas 7.4, 7.5, 7.7, 7.8, 7.9 are still valid.

In this case, still retaining a translation speed under 10 m/s it is possible to use a beam diameter of 0.02 cm with a pulse energy of 0.13 mJ, repetition rate of 52 kHz and therefore a total power that is lower than in the case of the Gaussian beam.

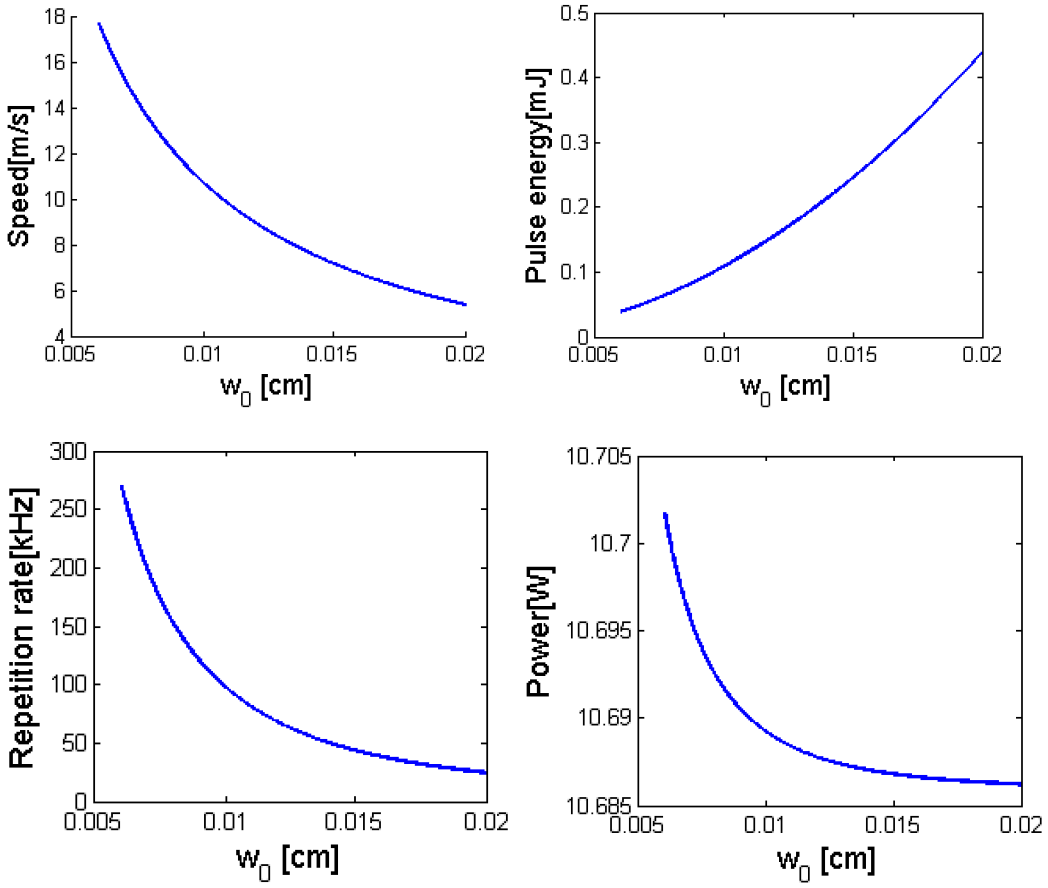

Figure 7.15: Translation speed of the beam, pulse energy, repetition rate and power of the source required for different waist values.

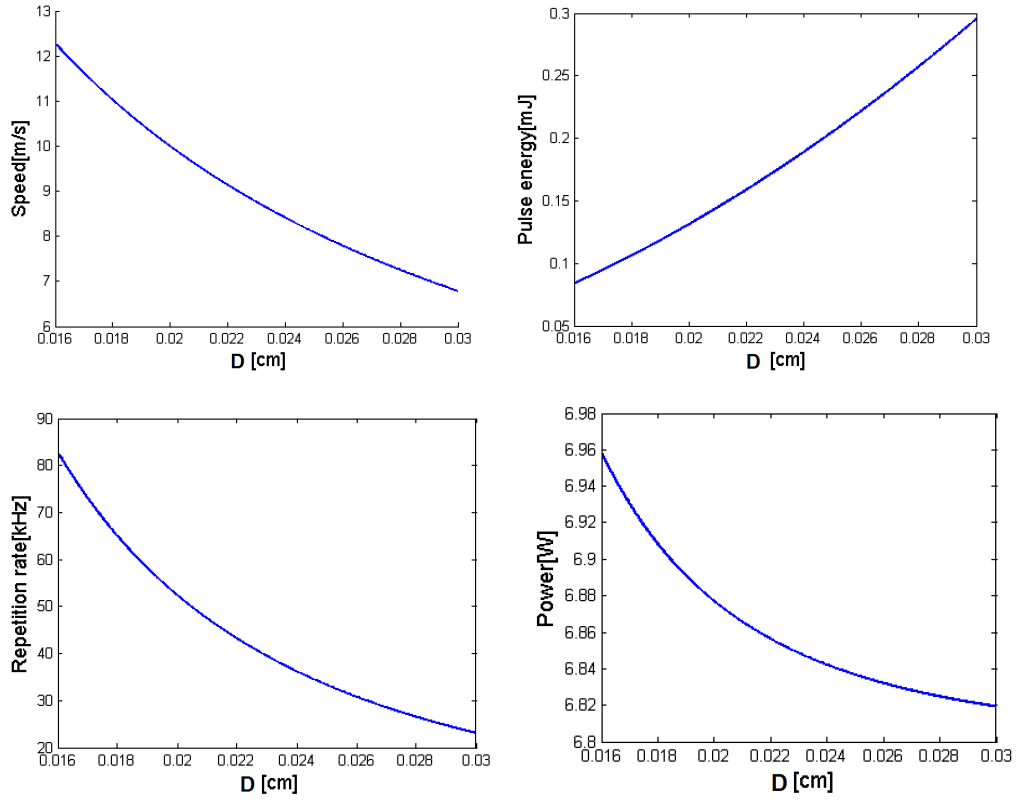

Figure 7.16: Translation speed of the beam, pulse energy, repetition rate and power of the source required in the case of flat-top beam.

Chapter 8

Conclusion.

This thesis work has studied the possible application of ultrafast lasers as sources for the opening of contacts on the passivation layer of the PERC photovoltaic cells. It is identified in the 'lift-off' process the phenomenon able to ensure better removal of the passivation material in non-texturized solar cells ensuring minimal damage to the adjacent areas at fluences significantly lower (hundreds of mJ/cm^2) compared to those typical of direct ablation of dielectric materials, over the J/cm^2.
In particular, we studied the dependence of the threshold fluence effect at different time length of the pulses (from 200 fs 10 ps), different average power (from 0 a 10 W) and roughness of the surface to be machined. The samples were subjected to SEM and EDX analysis showed the possibility to have a full delamination of the layer of interest.
In the case of surfaces with high roughness, typically textured surfaces, the phenomenon of indirect ablation in the considered regime has not led to a total removal of the passivating material, not allowing an optimal contacting of the final device, due to the greater active surface that reduces the effects of high intensity. A future development of this work may be the creation of a theoretical model that describes all the interaction processes with the material contributing to the phenomenon of indirect ablation. In the literature there are already several works that concern the interaction between ultrafast pulses and various materials, such as silicon, but it lacks a description of the phenomenon. In this way it would be possible to have a comparison between our experimental data on indirect ablation dependencies compared to the parameters of the laser source and the surface.
Finally, it would be extremely interesting to estimate the efficiency of cells without texture processed with ultrafast source so as to compare the electronic characteristics of the texturized cells already reported in this thesis.

Appendix A

Matlab analysis

This code was used to analyse the SEM images of spots and calculate the fluence threshold.

```
close all;
clear all;

%Scale of the image written by the SEM
scaleimage=[500,500,500,500,500,500,500,500,500,500];       %[um]
reprate=10000;                                              %[Hz]
numberROW=10;
Pmax=0.5;                       %[W] power of first row
Pspacing=0.01;                  %[W] power spacing between rows
range=0;                        %intensity to be added to ...
    the threshold, set 0 to not change it

%delete all the white pixels groups below this area while ...
    identifying the circles
minimumarea=round(80/500*scaleimage);

%open file to insert results
fileid=fopen('results.txt','w');
formatSpec = '   %s          %s       %s       %s       %s';
fprintf(fileid,formatSpec,'%','w0 [um]','sigma w0','F_th ...
    [mJ/cm^2]','sigma F_th');

%the images must have decreasing powers
name=[cellstr('5_.jpg'),cellstr('4_.jpg'), ...
    cellstr('3_.jpg'),cellstr('2_.jpg')];

for m=0:1:range %cycle for different depth
k=0;
n=0;
```

```
26 j=0;
27 l=m+1;
28 row4image(1)=0;
29
30 for i=1:1:length(name) %cycle on image
31
32     data = imread(char(name(i)));
33     data = rgb2gray(data);
34     figure(i);
35     imshow(data);
36
37     %find the length of scale bar to have the image scale ...
           factor
38     bottom=data(970,:);
39     black_scale=find(bottom==0);
40     scale=length(black_scale);
41     scalefactor=scaleimage(i)/scale;      %um/pixel
42
43     %delete the white band at bottom of the image
44     data=data(1:960,:);
45
46     % apply gaussian filter
47     H = fspecial('gaussian',5,3);
48     data = imfilter(data,H,'replicate');
49
50     data=data';
51
52     %convert to binary image and find boundaries in
53     Zmax=double(max(max(data)));
54     threshold(l) = graythresh(data);
55     threshold(l)=threshold(l)+(m/Zmax);
56     bw = im2bw(data,threshold(l));
57
58     %delete groups of pixels with low area, needed to ...
           reduce noise
59     bw = bwareaopen(bw,minimumarea(i));
60
61     [B,L] = bwboundaries(bw,'noholes');
62     numberSPOT=length(B);
63
64 j=1;
65 k=k+1;
66 last=0;
67 Area_mean(k,2)=0;
68 Center=0;
69 Radii=0;
70 Diameter=[0,0];
71 check=0;
72 Center2=0;
```

```
73 Radii2=0;
74
75  for n=1:1:numberSPOT
76
77      %extremes of the spot
78      MINX=min(B{n,1}(:,1))-10;       %X=rows
79      MAXX=max(B{n,1}(:,1))+10;
80      MINY=min(B{n,1}(:,2))-10;       %Y=columns
81      MAXY=max(B{n,1}(:,2))+10;
82      A=[MINX,MINY;MAXX,MAXY];
83
84     %if the spot is too near the edge of the image
85     % it does not get accepted because it could be incompleted
86  if((A(:,1)>0) & (A(:,1)<size(data,1)) & (A(:,2)>0) & ...
       (A(:,2)<size(data,2)))
87
88      %cut the spot from the image to analyze it
89      spot=bw(MINX:MAXX,MINY:MAXY);
90
91      %find the pixles which constitutes the spot
92      [row,col]=find(spot==1);
93
94      Center(j,1)=(MINX+MAXX)/2;
95      Center(j,2)=(MINY+MAXY)/2;
96      Diameter(j,:)=[MAXY,MINY];
97
98      %check whether the center of the spot is inside the
99      %diameter of the previous one, in this way if it is
100     %they are on the same row even if the image has
101     % a slight slope. The first spot is excluded from ...
           this check.
102
103     if (j>1 & Center(j,2)>Diameter(j-1,2) & ...
           Center(j,2)<Diameter(j-1,1))
104        Area_mean(k,2)=Area_mean(k,2)+length(row);
105     else if (j==1) %reserved for the first spot of each image
106                 Area_mean(k,2)=length(row);
107          else
108        %if the cascade has conducted here the spot must be
109        %from a new row so we must check the correctness
110        %of the previous row
111             if (j-1-last>5)
112             % the row is not accepted if there are not enough
113             %spot, at least 5 are needed
114                 Area_mean(k,1)=Pmax-Pspacing*(k-1);% beam ...
                       power
115                 Area_mean(k,2)=(Area_mean(k,2)/(j-1-last)) ...
                       .*scalefactor^2;
116                 residual(k,1:(j-1-last))=Area_mean(k,2)- ...
```

```
                    (Area(k,1:(j-1-last)).*scalefactor^2);
117                 Area_mean(k,3)=sqrt(sum( ...
                    residual(k,1:(j-1-last)).^2) ...
                    /(j-1-last));      %mean error
118                 if (Area_mean(k,3)/Area_mean(k,2))>0.15
119                 %the row is invalid if the percentual error
120                 % of the mean area is over 15%,
121                  %because sometimes spots that
122                 %do not exist are added to a row
123                    Area_mean(k,:)=0;
124                  else
125                 %the spots, if the full row is accepted, get
126                 %their number record to be plotted
127                      check=[check, ...
                        linspace(last+1,j-1,(j-1-last))];
128                  end
129                  last=j-1;
130                  k=k+1;
131                  Area_mean(k,2)=length(row);
132               else
133                  Area_mean(k,2)=length(row);
134                   last=j-1;
135                   end
136               end
137           end
138          %calculate area and radius of the single spot
139          Area(k,j-last)=length(row);
140          Radii(j)=sqrt(Area(k,j-last)/pi);
141          j=j+1;
142     end
143   end
144
145     %The last spot must check to ensure that the row is valid
146     if (j-1-last>5)
147         Area_mean(k,1)=Pmax-Pspacing*(k-1);
148         Area_mean(k,2)=(Area_mean(k,2)/ ...
            (j-1-last)).*scalefactor^2;
149         residual(k,1:(j-1-last))=Area_mean(k,2)- ...
            (Area(k,1:(j-1-last)).*scalefactor^2);
150         Area_mean(k,3)=sqrt(sum( ...
            residual(k,1:(j-1-last)).^2)/(j-1-last));
151         if (Area_mean(k,3)/Area_mean(k,2))>0.15
152             Area_mean(k,:)=0;
153         else check=[check,linspace(last+1,j-1,(j-1-last))];
154         end
155     else
156         Area_mean(k,:)=[];
157         Area(k,:)=[];
158         k=k-1;
```

```
159     end
160
161     %cycle needed to write only the spot of correct rows
162     for index=2:1:length(check)
163         Center2(index-1,1)=Center(check(index),1);
164         Center2(index-1,2)=Center(check(index),2);
165         Radii2(index-1)=Radii(check(index));
166     end
167    %if there's at least one correct row we plot red ...
          circles of the measured
168    %radius
169    if length(Radii2)>1
170     viscircles(Center2,Radii2);
171    end
172 end
173
174 % Delete from area_mean(:,2) the rows which do not get ...
      accepted because
175 %the error is too high, they where labeled as 0 before.
176 over15=find(Area_mean(:,2)==0);
177 for ind=1:1:length(over15)
178     cut=over15(ind)-ind+1;
179     Area_mean(cut,:)=[];
180 end
181 % plot to check how goes the error
182 error=Area_mean(:,3)*100./Area_mean(:,2);
183 figure(200)
184 plot(error(:),'.');
185
186 %rewrite the data gained from the image analysis in the ...
      correct units for
187 %the next analysis
188 Dsquare(:,1)=Area_mean(:,1);                    %[W]
189 Dsquare(:,2)=(4.*Area_mean(:,2)./pi);           %[um^2]
190 Dsquare(:,3)=4.*Area_mean(:,3)./pi;             %D^2 error
191
192
193 %Fluence analysis
194
195 %linear interpolation
196 x=log(Dsquare(:,1));
197 t(1)=60;
198 t(2)=200;
199 [a,Res,Jacob,CovB]= nlinfit(x(:),Dsquare(:,2),@fitlinear,t);
200 SOL=a(1)*x(:)+a(2);
201
202 %Extrapolate W_0, threshold power and threshold fluence
203 w0(l)=sqrt(a(1)/2);       %[um]
204 P_th(l)=exp(-a(2)/a(1));         %[W]
```

```
205 F_th(l)=1e11*(P_th(l)/reprate)/(pi*w0(l)^2);  %[mJ/cm^2]
206
207 sigma1=sqrt(CovB(1,1));              %error a(1)
208 sigma2=sqrt(CovB(2,2));              %error a(2)
209
210 %propagation to values
211 sigma_w(l)=0.5*sqrt(1/(2*a(1)))*sigma1;
212 sigma_p(l)=P_th(l)*sqrt((sigma2/a(1))^2+ ...
        (a(2)*sigma1/(a(1)^2))^2);
213 sigma_f(l)=sqrt((F_th(l)*sigma_p(l)/P_th(l))^2+ ...
        (2*F_th(l)*sigma_w(l)/w0(l))^2);
214
215 %calculate fluence for each row to plot
216 F=1e11*(Dsquare(:,1)/reprate)/(pi*w0(l)^2);
217
218 % Create figure
219 figure1 = figure;
220
221 %Create axes
222 axes1 = axes('Parent',figure1,...
223     'XScale','log',...
224     'XMinorTick','on');
225 xlabel('Fluence [J/cm^2]','FontSize',18);
226 ylabel('D^2 [um^2]','FontSize',18);
227 box(axes1,'on');
228 hold(axes1,'all');
229
230 semilogx1 = semilogx(F,Dsquare(:,2),F,SOL);
231 set(semilogx1(1),'MarkerSize',5,'Marker','square', ...
        'LineStyle','none', 'MarkerEdgeColor','black', ...
        'MarkerFaceColor','black');
232
233 %write values in results.txt
234 formatSpec = '\n%6.3f        %6.3f        %6.3f ...
                  %6.3f            %6.3f';
235 fprintf(fileid,formatSpec,threshold(l)*100, ...
        w0(l),sigma_w(l),F_th(l),sigma_f(l));
236
237 %for safety reason when you have a range greater than 0, ...
        not needed
238 clear Area_mean;
239 clear Dsquare;
240
241 end
242
243 %graph of different fluence threshold for various range
244 figure(1000),
245 errorbar(threshold.*100,F_th,sigma_f,'.','MarkerSize',10)
246 xlabel('Threshold [%]','FontSize',18)
```

```
247 ylabel('Fluence [J/cm^2]','FontSize',18);
248
249 fclose(fileid); %close results file
```

Bibliography

[1] R Ramponi, R Osellame, and G Cerullo. *Femtosecond Laser Micromachining*, volume 123 of *Topics in Applied Physics*. Springer Berlin Heidelberg, Berlin, Heidelberg, 2012.

[2] R Stoian, D Ashkenasi, A Rosenfeld, and E E B Campbell. Coulomb explosion in ultrashort pulsed laser ablation of Al 2 O 3. 62(19):167–173, 2000.

[3] Fei He, Yang Liao, Jintian Lin, Jiangxin Song, Lingling Qiao, Ya Cheng, and Koji Sugioka. Femtosecond laser fabrication of monolithically integrated microfluidic sensors in glass. *Sensors (Basel, Switzerland)*, 14(10):19402–40, January 2014.

[4] LV Keldysh. Ionization in the field of a strong electromagnetic wave. *Sov. Phys. JETP*, 20(5):1307–1314, 1965.

[5] B. C. Stuart, M. D. Feit, S. Herman, a. M. Rubenchik, B. W. Shore, and M. D. Perry. Optical ablation by high-power short-pulse lasers. *Journal of the Optical Society of America B*, 13(2):459, February 1996.

[6] J. D. Jackson. Classical Electrodynamics, 3rd ed. *American Journal of Physics*, 67(9):841, September 1999.

[7] N.M. Bulgakova, R. Stoian, a. Rosenfeld, I.V. Hertel, W. Marine, and E.E.B. Campbell. A general continuum approach to describe fast electronic transport in pulsed laser irradiated materials: The problem of Coulomb explosion. *Applied Physics A*, 81(2):345–356, April 2005.

[8] X Jia, T Q Jia, Y Zhang, P X Xiong, D H Feng, Z R Sun, J R Qiu, and Z Z Xu. Periodic nanoripples in the surface and subsurface layers in ZnO irradiated by femtosecond laser pulses. *Optics letters*, 35(8):1248–50, April 2010.

[9] M. Malinauskas, P. Danilevičius, D. Baltriukien, M. Rutkauskas, A. Žukauskas, Ž. Kairyt, G. Bičkauskait, V. Purlys, D. Paipulas, V. Bukelskien, and R. Gadonas. 3D artificial polymeric scaffolds for stem cell growth fabricated by femtosecond laser. *Lithuanian Journal of Physics*, 50(1):75–82, 2010.

[10] BN Chichkov, C Momma, and S Nolte. Femtosecond, picosecond and nanosecond laser ablation of solids. *Applied Physics A*, 115:109–115, 1996.

[11] N Bärsch, K Körber, A Ostendorf, and KH Tönshoff. Ablation and cutting of planar silicon devices using femtosecond laser pulses. *Applied Physics A*, 242:237–242, 2003.

[12] E Steiger, M Scharnagl, and M Kemnitzer. Micro-processing and structuring of Si and CIS thin-film solar cells with an ultrafast picosecond laser. pages 3–8.

[13] T. Rublack, S. Hartnauer, P. Kappe, C. Swiatkowski, and G. Seifert. Selective ablation of thin SiO2 layers on silicon substrates byfemto- and picosecond laser pulses. *Applied Physics A*, 103(1):43–50, March 2011.

[14] Philip Jackson, Dimitrios Hariskos, Erwin Lotter, Stefan Paetel, Roland Wuerz, Richard Menner, Wiltraud Wischmann, and Michael Powalla. New world record efficiency for Cu(In,Ga)Se2 thin-film solar cells beyond 20%. *Progress in Photovoltaics: Research and Applications*, 19(7):894–897, November 2011.

[15] Andrew W. Blakers, Aihua Wang, Adele M. Milne, Jianhua Zhao, and Martin a. Green. 22.8% Efficient Silicon Solar Cell. *Applied Physics Letters*, 55(13):1363, 1989.

[16] Joseph Mandelkorn. A new electric field effect in silicon solar cells. *Journal of Applied Physics*, 44(10):4785, 1973.

[17] Joseph Mandelkorn and John H. Lamneck. Simplified fabrication of back surface electric field silicon cells and novel characteristics of such cells. *Solar Cells*, 29(2-3):121–130, August 1990.

[18] S. Narasimha, A. Rohatgi, and A.W. Weeber. An optimized rapid aluminum back surface field technique for silicon solar cells. *IEEE Transactions on Electron Devices*, 46(7):1363–1370, July 1999.

[19] Elias Urrejola, Kristian Peter, Heiko Plagwitz, and Gunnar Schubert. Al–Si alloy formation in narrow p-type Si contact areas for rear passivated solar cells. *Journal of Applied Physics*, 107(12):124516, 2010.

[20] Daniel Kray, Sybille Hopman, Akos Spiegel, Bernold Richerzhagen, and Gerhard P. Willeke. Study on the edge isolation of industrial silicon solar cells with waterjet-guided laser. *Solar Energy Materials and Solar Cells*, 91(17):1638–1644, October 2007.

[21] G. Poulain, D. Blanc, A. Focsa, M.De Vita, B. Semmache, M. Gauthier, Y. Pellegrin, and M. Lemiti. Laser Ablation Mechanism Of Silicon Nitride Layers In A Nanosecond UV Regime. *Energy Procedia*, 27:516–521, January 2012.

[22] K. Stolberg. Ablation of SiN Passivation Layers on Photovoltaic Cells with Femtosecond Laser Source. *Journal of Laser Micro/Nanoengineering*, 5(2):125–127, July 2010.

[23] Sonja Hermann, Tara Dezhdar, Nils-Peter Harder, Rolf Brendel, Michael Seibt, and Sandra Stroj. Impact of surface topography and laser pulse duration for laser ablation of solar cell front side passivating SiN[sub x] layers. *Journal of Applied Physics*, 108(11):114514, 2010.

[24] Tino Rublack, Martin Schade, Markus Muchow, Hartmut S. Leipner, and Gerhard Seifert. Proof of damage-free selective removal of thin dielectric coatings on silicon wafers by irradiation with femtosecond laser pulses. *Journal of Applied Physics*, 112(2):023521, 2012.

[25] Gerrit Heinrich and Alexander Lawerenz. Non-linear absorption of femtosecond laser pulses in a SiNx layer—influence of silicon doping type. *Solar Energy Materials and Solar Cells*, 120:317–322, January 2014.

[26] Bruce A. Garetz and Stephen Arnold. Variable frequency shifting of circularly polarized laser radiation via a rotating half-wave retardation plate. *Optics Communications*, 31(1):1–3, October 1979.

[27] A Yariv, Y Amnon, and Y Pochi. *Photonics-Optical electronics in modern communications*. Oxford University Press, Inc., 2006.

[28] Rick Trebino. The Measurement of Ultrashort Laser Pulses. *Frontiers in Optics*, page SC155, 2005.

[29] Hatem Dachraoui and Wolfgang Husinsky. Thresholds of Plasma Formation in Silicon Identified by Optimizing the Ablation Laser Pulse Form. *Physical Review Letters*, 97(10):107601, September 2006.

[30] Patrick Lorazo, Laurent Lewis, and Michel Meunier. Thermodynamic pathways to melting, ablation, and solidification in absorbing solids under pulsed laser irradiation. *Physical Review B*, 73(13):134108, April 2006.

[31] a. a. Ionin, S. I. Kudryashov, L. V. Seleznev, D. V. Sinitsyn, a. F. Bunkin, V. N. Lednev, and S. M. Pershin. Thermal melting and ablation of silicon by femtosecond laser radiation. *Journal of Experimental and Theoretical Physics*, 116(3):347–362, April 2013.

[32] Senthilnathan Panchatsharam, Bo Tan, and Krishnan Venkatakrishnan. Femtosecond laser-induced shockwave formation on ablated silicon surface. *Journal of Applied Physics*, 105(9):093103, 2009.

[33] Patrick Lorazo, Laurent J Lewis, and Michel Meunier. Short-pulse laser ablation of solids: from phase explosion to fragmentation. *Physical review letters*, 91:225502, 2003.

[34] N. a. Inogamov, V. V. Zhakhovskii, S. I. Ashitkov, Yu. V. Petrov, M. B. Agranat, S. I. Anisimov, K. Nishihara, and V. E. Fortov. Nanospallation induced by an ultrashort laser pulse. *Journal of Experimental and Theoretical Physics*, 107(1):1–19, August 2008.

[35] Justin Henrie, Spencer Kellis, Stephen M Schultz, and Aaron Hawkins. Electronic color charts for dielectric films on silicon. 12(7):1464–1469, 2004.

[36] Gerrit Heinrich, Mario Bähr, Klaus Stolberg, Tobias Wütherich, Marcel Leonhardt, and Alexander Lawerenz. Investigation of ablation mechanisms for selective laser ablation of silicon nitride layers. *Energy Procedia*, 8:592–597, January 2011.

[37] Jonas Krause, Robert Woehl, Michael Rauer, Christian Schmiga, Jürgen Wilde, and Daniel Biro. Microstructural and electrical properties of different-sized aluminum-alloyed contacts and their layer system on silicon surfaces. *Solar Energy Materials and Solar Cells*, 95(8):2151–2160, August 2011.

[38] Daisuke Niinobe, Hiroaki Morikawa, Shuichi Hiza, Takehiko Sato, Shigeru Matsuno, Hirofumi Fujioka, Tomotaka Katsura, Tatsuki Okamoto, Satoshi Hamamoto, Takashi Ishihara, and Satoshi Arimoto. Large-size multi-crystalline silicon solar cells with honeycomb textured surface and point-contacted rear toward industrial production. *Solar Energy Materials and Solar Cells*, 95(1):49–52, January 2011.